# Iterated stretching of viscoelastic jets

Hsueh-Chia Chang,[a)] Evgeny A. Demekhin, and Evgeny Kalaidin
*Department of Chemical Engineering, University of Notre Dame, Notre Dame, Indiana 46556*

We examine, with asymptotic analysis and numerical simulation, the iterated stretching dynamics of FENE and Oldroyd-B jets of initial radius $r_0$, shear viscosity $\nu$, Weissenberg number $We$, retardation number $S$, and capillary number $Ca$. The usual Rayleigh instability stretches the local uniaxial extensional flow region near a minimum in jet radius into a primary filament of radius $[Ca(1-S)/We]^{1/2}r_0$ between two beads. The strain-rate within the filament remains constant while its radius (elastic stress) decreases (increases) exponentially in time with a long elastic relaxation time $3We(r_0^2/\nu)$. Instabilities convected from the bead relieve the tension at the necks during this slow elastic drainage and trigger a filament recoil. Secondary filaments then form at the necks from the resulting stretching. This iterated stretching is predicted to occur successively to generate high-generation filaments of radius $r_n$, $(r_n/r_0)=\sqrt{2}(r_{n-1}/r_0)^{3/2}$ until finite-extensibility effects set in. © *1999 American Institute of Physics.* [S1070-6631(99)01307-0]

## I. INTRODUCTION

There has been considerable recent progress in our understanding of Newtonian jet dynamics. Numerical simulation can now significantly extend the classical linear Rayleigh theory for the initial small-amplitude evolution.[1] However, singular stresses that occur as the jet radius approaches zero have prevented accurate numerical resolution of the final breakup dynamics. Instead, recent mathematical analysis of the self-similar, finite-time singularity formation near breakup has provided significant insight,[2–7] including an interesting study of observed iterated jet pinching leading to breakup.[5] Universal scalings of the near-breakup evolution are now well understood, eventhough the longwave approximation invoked in the theory may prevent it from resolving the dynamics at or beyond breakup when drops begin to form. The hope is that one can ''patch'' the breakup analysis for the numerically inaccessible interval to numerical simulation of the evolution prior and beyond breakup. Since there are only a few parameters in the governing equations, delineation by numerical simulation can be readily carried out away from the breakup stage.

Such a luxury is lost in another classical jet breakup problem—evolution of non-Newtonian jets. In addition to the usual capillary forces that drive the breakup, viscoelasticity effects introduced by polymers are known to significantly alter the breakup dynamics. However, viscoelasticity not only introduces additional rheological parameters but also renders the equations hyperbolic. Both factors exclude exhaustive numerical analysis even with modern-day computers. In any case, the myriad of physical effects introduced by the polymers can probably be best elucidated with an analysis that can isolate each effect.

Linear stability analysis that amounts to an extension of the classical Rayleigh theory can be readily carried out for viscoelastic jets. However, since viscoelastic effects can only be triggered when the polymers are significantly stretched by the flow, viscoelasticity is not expected to be of significance initially when the flow within the unperturbed jet of radius $r_0$ is either zero or a uniform axial flow. Prior linear theories[8,9] indeed confirm that viscoelasticity does not alter the classical Rayleigh wavelength $2\sqrt{2}\pi r_0$ significantly and only slightly increases the growth rate.

However, as uniaxial extensional disturbance flows are created by the initial disturbance, the polymers are stretched considerably at the stagnation points and the late-stage dynamics are profoundly affected by viscoelasticity. Experiments[8] show that the breakup is delayed by orders of magnitude. In some cases, the viscoelastic jet may not even break up over the entire duration of the experiment. Instead of pinching asymmetrically about the pinch point like a Newtonian jet to form satellites, a unique filament-bead configuration is observed. This configuration is extremely robust and the drainage from the stretched filament to the compressed beads is extremely slow. If the viscoelastic jet does break, it breaks at the necks joining the filament to the beads. This bead-filament configuration has also been observed in numerical simulation by Bousfield etc.[10] for an Oldroyd-B fluid. Due to the slow drainage from the filament, the simulation is unable to proceed beyond the bead-filament configuration and determine the final fate of the jet.

Instead, a number of theoretical analyses have focused on the breakup dynamics of slender filaments.[11–13] These theories[11,12] have uncovered the exponential drainage dynamics of an elastic filament. This drainage is driven by the capillary pressure difference between the bead and filament. A more detailed force and mass balance across this neck will be offered here but the scalings of earlier elastic drainage theories remain valid. Because the radii of both bead and filament vary very slowly, the constant capillary driving force approximation is valid quasi-steadily. The reason both radii vary slowly, on the other hand, is because the elastic

[a)]Electronic mail: hsueh-chia.chang.2@nd.edu

1717

axial stress, created by the stretched polymers during filament drainage, exactly cancels the slowly varying capillary pressure. As a result, a linear uniaxial extensional flow exists within the filament with a constant strain-rate. Due to the drainage, the filament radius decreases and the axial stress increases but the strain-rate remains constant. This unique drainage mechanism yields a distinctive exponential decrease in time for the filament radius with a large elastic time scale. The exponential thinning implies that an Oldroyd-B jet, in contrast to the Newtonian case, does not breakup in finite time. It is only when finite extensibility in a FENE model is introduced that finite-time breakup is predicted.

However, these analyses omit inertial effects and focus only on slender filaments. Since the Newtonian self-similar breakup solution of Eggers[3] involves inertia, it is not clear that its omission is valid in late-stage filament dynamics with fast axial flow. More importantly, experimental data for Newtonian jets[5] and non-Newtonian jets[8] clearly show that much of the late-stage jet dynamics, including breakup, occur at the neck joining the filament to the bead. For example, iterated pinching has been observed in Newtonian jets[5] at the necks. Such dynamics escape the analyses of Renardy[11] and Entov and Hinch[12] for slender filaments without inertia. Important dynamics at the neck of the jets have hence escaped our understanding thus far. In this report, we endeavor to delineate both the formation mechanism for the bead-filament configuration and the dynamics at the necks. We shall examine both an Oldroyd-B jet and a FENE jet and reveal an interesting recoil and iterated stretching dynamics.

## II. LONGWAVE SIMPLIFICATION AND SIMULATION

We use the FENE-CR model of Chilcott and Rallison,[14] a simplification of the classical FENE dumbbell model,[15] to determine the stress tensor

$$\tau = \mu_s \dot{\gamma} + G f(R)(\mathbf{A} - \mathbf{I}), \tag{1}$$

where $R^2 = $ trace $\mathbf{A}$. The spring force law with

$$f(R) = \frac{1}{1 - R^2/L^2}, \tag{2}$$

represents finite extensibility with $L$ as the ratio of the length a fully extended dumbell to its equilibriu length and $\mathbf{A}$ being the ensemble average of the dyadic product of the end-to-end vector of the dumbbell, normalized by the equilibrium separation. The matrix $\mathbf{A}$ is taken to evolve by

$$\frac{\partial \mathbf{A}}{\partial t} + u \cdot \nabla \mathbf{A} = \mathbf{A} \cdot \nabla u + \nabla u^T \cdot \mathbf{A} - \frac{f(R)}{D}(\mathbf{A} - \mathbf{I}). \tag{3}$$

The parameters $\mu_s$, $G$, and $D$ represent solvent viscosity, elastic modulus, and relaxation time $D$, respectively. The magnitude of non-Newtonian stresses is measured by $c = GD/\mu_s$ such that the steady shear viscosity $\dot{\nu} = (1 + c)\mu_s/\rho$. The tensor $\dot{\gamma} = \nabla \mathbf{u} + (\nabla \mathbf{u})^T$ is the rate-of-strain tensor.

The appropriate boundary conditions are the normal and tangential balances at the jet interface defined by $r = h(z)$. There is also the kinematic condition for mass conservation

$$\frac{\partial h^2}{\partial t} + \frac{\partial}{\partial z} \int_0^h 2rudr = 0. \tag{4}$$

In the longwave limit when $h(z)$ varies slowly with respect to $z$, the axial velocity, pressure, and the stress components $\tau_{zz}$ and $\tau_{rr}$ are almost uniform with respect to $r$ while the radial velocity $v$ and the off-diagonal stress components $\tau_{rz}$ and $\tau_{zr}$ are nearly zero. Hence, the proper ansatz for slender jets is a Taylor expansion in $r$

$$u \sim u_0 + u_2 r^2 \cdots, \tag{5a}$$

$$v \sim -\frac{1}{2}\frac{\partial u_0}{\partial z}r - \frac{1}{4}\frac{\partial u_2}{\partial z}r^3 \cdots, \tag{5b}$$

$$p \sim p_0 + p_2 r^2 + \cdots, \tag{5c}$$

$$\tau_{zz} \sim \tau_{zz}^0 + \cdots, \tag{5d}$$

$$\tau_{rz} = \tau_{zr} \sim Tr + \cdots, \tag{5e}$$

$$\tau_{rr} \sim \tau_{rr}^0 + \cdots, \tag{5f}$$

$$A_{zz} \sim A_{zz}^0, \tag{5g}$$

$$A_{rz} = A_{zr} \sim A_{rz}^0 r, \tag{5h}$$

$$A_{rr} \sim A_{rr}^0, \tag{5i}$$

where all the coefficients of expansion are only function of $t$ and $z$.

Upon substituting this ansatz into the equations of motion and boundary conditions, nondimensionalizing with the initial undisturbed radius $r_0$ as the characteristic length $r_0^2/\nu$ as the characteristic time, where $\nu = \mu_s(1+c)/\rho$ is the shear viscosity due to both solvent and polymer, and $\nu/r_0$ as the characteristic velocity, one gets to leading order in $r$, with uniform pressure and axial flow and negligible off-diagonal stresses, the following dimensionless longwave equations:

$$\frac{\partial u}{\partial t} + u\frac{\partial u}{\partial z} = \frac{1}{Ca}\frac{\partial \kappa}{\partial z} + \frac{1}{h^2}\frac{\partial}{\partial z}[h^2(\tau_{zz} - \tau_{rr})], \tag{6a}$$

$$\frac{\partial h^2}{\partial t} + \frac{\partial}{\partial z}(h^2 u) = 0, \tag{6b}$$

$$\frac{\partial A}{\partial t} + \frac{\partial}{\partial z}(uA) - 3A\frac{\partial u}{\partial z} + \frac{f(R)}{We}(A - 1) = 0, \tag{6c}$$

$$\frac{\partial B}{\partial t} + \frac{\partial}{\partial z}(uB) + \frac{f(R)}{We}(B - 1) = 0, \tag{6d}$$

$$\tau_{zz} = 2S\frac{\partial u}{\partial z} + \frac{1 - S}{We}f(R)(A - 1), \tag{6e}$$

$$\tau_{rr} = -S\frac{\partial u}{\partial z} + \frac{1 - S}{We}f(R)(B - 1), \tag{6f}$$

where $u$ denotes $u_0$, $\kappa$ the jet curvature, the radially uniform axial velocity, $A$ and $B$ represent the polymer stretching in the axial and radial directions, $A_{zz}^0$ and $A_{rr}^0$, respectively, and $\tau_{zz}$ and $\tau_{rr}$ the dimensionless versions of their counterparts

in Eq. (5) with a superscript 0. All these quantities are functions of the dimensionless $z$ and $t$ only. The spring law Eq. (2) now becomes

$$f(R) = \frac{L^2}{L^2 - (A+B)}, \tag{7}$$

and the other parameters are the usual capillary, Weissenberg and retardation numbers $Ca = \rho \nu^2 / \sigma r_0$, $We = D\nu/r_0^2$ and $S = 1/(1+c)$.

The parameter $We$ measures the elasticity of the polymers related to the relaxation time $D$. We are interested in the strongly elastic limit with $We \gg 1$. The retardation parameter $S$, on the other hand, is associated with the ratio of retardation time scale due to non-Newtonian stress to the relaxation time scale $D$. It is bounded between zero (Newtonian limit) and unity. The capillary number is also a unit-order parameter relative to $We$. We shall be exploiting the smallness of $We^{-1}$ in subsequent asymptotic analyses. The extensibility parameter $L$, on the other hand, can range from unit order to $O(We)$, depending on the molecular weight,[16] with $L \to \infty$ being the Oldroyd-B limit.

To render the hyperbolicity of the stress constitutive equations more apparent, it is convenient to separate the polymer elastic stress from the quasi-viscous retardation stress by defining the excess stresses

$$\hat{\tau}_{zz} = \tau_{zz} - 2S \frac{\partial u}{\partial z} \quad \text{and} \quad \hat{\tau}_{rr} = \tau_{rr} + S \frac{\partial u}{\partial z}, \tag{8}$$

to remove the velocity derivative in time in the stress equations that result when Eqs. (6c)–(6f) are combined. The resulting equations are

$$\frac{\partial u}{\partial t} + u \frac{\partial u}{\partial z} = \frac{1}{Ca} \frac{\partial \kappa}{\partial z} + \frac{1}{h^2} \frac{\partial}{\partial z} [h^2 (\hat{\tau}_{zz} - \hat{\tau}_{rr})]$$
$$+ \frac{3S}{h^2} \frac{\partial}{\partial z} \left( h^2 \frac{\partial u}{\partial z} \right), \tag{9a}$$

$$\frac{\partial h^2}{\partial t} + u \frac{\partial h^2}{\partial z} + \frac{\partial u}{\partial z} h^2 = 0, \tag{9b}$$

$$\frac{\partial A}{\partial t} + u \frac{\partial A}{\partial z} - 2A \frac{\partial u}{\partial z} + \frac{f(R)}{We} (A-1) = 0, \tag{9c}$$

$$\frac{\partial B}{\partial t} + u \frac{\partial B}{\partial z} + B \frac{\partial u}{\partial z} + \frac{f(R)}{We} (B-1) = 0, \tag{9d}$$

$$\hat{\tau}_{zz} = \frac{1-S}{We} f(R)(A-1), \tag{9e}$$

$$\hat{\tau}_{rr} = \frac{1-S}{We} f(R)(B-1). \tag{9f}$$

The inertial terms lie to the left of the equation of motion [Eq. (9a)] and they are balanced by the capillary pressure gradient, the gradient of the normal stress difference and the polymer retardation stress terms on the right. The constitutive equations [Eqs. (9c)–(9e)], capture the convection of the

stresses along the streamline, the stretching due to the velocity gradient ($\partial u/\partial z$), finite extensibility in $f(R)$ and the relaxation of the stretched polymers.

Several limits of Eq. (9) can be readily derived. The extensibility $L$ is practically infinite when $(A+B) \ll L^2$ in Eq. (7). In this limit, Eqs. (9e) and (9f) yield the Hookean spring laws

$$A = 1 + \hat{\tau}_{zz} \frac{We}{(1-S)} \quad \text{and} \quad B = 1 + \hat{\tau}_{rr} \frac{We}{(1-S)}, \tag{10}$$

and, upon substitution into Eqs. (9c) and (9d), the stress evolution of an Oldroyd-B fluid results

$$\frac{\partial}{\partial t} \hat{\tau}_{zz} + u \frac{\partial}{\partial z} \hat{\tau}_{zz} - 2 \hat{\tau}_{zz} \frac{\partial u}{\partial z} + \frac{1}{We} \left\{ \hat{\tau}_{rr} + 2(S-1) \frac{\partial u}{\partial z} \right\} = 0, \tag{11a}$$

$$\frac{\partial}{\partial t} \hat{\tau}_{rr} + u \frac{\partial}{\partial z} \hat{\tau}_{rr} + \hat{\tau}_{rr} \frac{\partial u}{\partial z} + \frac{1}{We} \left\{ \hat{\tau}_{rr} - (S-1) \frac{\partial u}{\partial z} \right\} = 0. \tag{11b}$$

The Oldroyd-B limit is hence not a singular limit.

If one further neglects elastic and retardation effects, $We = 0$ and $S = 0$, a Newtonian limit is obtained with $\hat{\tau}_{zz} = -(2\partial u/\partial z)$ and $\hat{\tau}_{rr} = -(\partial u/\partial z) \sim -2(\partial v/\partial r)$.

It is far simpler to integrate the longwave equation Eq. (9) or Eq. (11) than the full equations of motion. However, strictly speaking, the longwave equation is only valid for filaments whose radii vary gradually. This is not true at the observed beads which are spherical. Nevertheless, the spherical beads should obey the axisymmetric Laplace–Young equation with constant curvature to leading order. Hence, if we retain the full curvature in Eq. (9a)

$$\kappa = \frac{h_{zz}}{(1+h_z^2)^{3/2}} - \frac{1}{h(1+h_z^2)^{1/2}}, \tag{12}$$

the spherical beads would also be captured to leading order by Eq. (9). We have successfully applied this composite approach to capture both the bead and annular film during drop formation when a vertical fiber is coated[17] and to capture both the finger tip and the thin wetting films in the Bretherton problem of air fingers replacing liquid in capillaries and channels.[18] It is nevertheless an *ad hoc* approach that is only valid to leading order. It must be verified against numerical simulation of the full equations to examine if there is any discrepancy due to higher order effects.

To this end, we compare in Fig. 1 our computed profiles from Eq. (11) for the Oldroyd-B fluid ($L \to \infty$) at $Ca = 10$, $We = 300$, and $S = 0.25$ in a domain of size $l = 20$ to the computation of the full equations by Bousfield *et al.*[10] Due to a different scaling, their dimensionless time $\theta$ corresponds to $t/Ca$ and their length corresponds to $z/l$ of the present notation. The results are presented in $\theta$ and $z/l$. As is evident, the evolution is faithfully captured by the longwave equation even after the bead-filament configuration is established. Our simulation of the Newtonian jet ($We = 0$) is also in agreement with earlier simulations by Eggers,[2,3] Papageorgiou,[4] and Brenner *et al.*[6]

As is consistent with the experiments, the longer simulations allowed by the longwave simplification reveal impor-
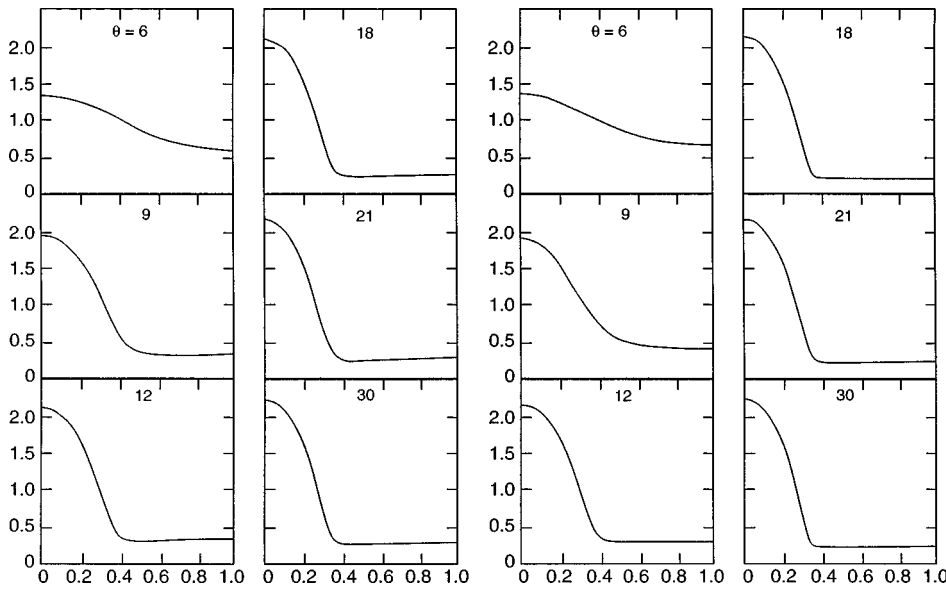
FIG. 1. Simulation of the jet radius $h(z,t)$ of the Oldroyd-B jet from the long-wave equation on the right and from the full equations of motion on the left by Bousfield *et al.* (Ref. 10). The parameters are $Ca=10$, $S=0.25$, $We=300$, and a domain size of $l=20$. The graphs are plotted in and axial scale of $z/l$ and a time scale of $t/Ca$.

tant jet dynamics at the necks joining the beads to the filament. Such late-stage dynamics develop long after the formation of the bead-filament configuration and is missed by earlier numerical studies. An extreme case of $We=10\,000$ is shown in Fig. 2. When the retardation number $S$ is not near its two limits of zero and unity, a distinctive recoil of the filament develops at the necks. The simulated evolution begins with the formation of a minimum in the jet radius due to the usual Rayleigh capillary instability. This creates a stagnation point at the minimum and an uniaxial extensional flow near it. The extensional flow stretches the polymers and generates elastic stresses of positive $\hat{\tau}_{zz}$ and negative $\hat{\tau}_{rr}$. The profiles of $\hat{\tau}_{zz}$ during the evolution are seen in Fig. 3. This axial elastic stress develops a symmetric maximum at the first stagnation point. As the jet profile near this point is stretched into a filament bounded by two beads at $t=6.5$, the stress profile evolves into a constant value within the fila-

ment. As pinching begins symmetrically at the two necks near $t=7.0$, two additional uniaxial extensional flows are created locally at the necks and the stress again exhibits two sharp maxima. The excess axial stress plays an important role in the recoil process.

The recoil that follows the pinching is shown in Figs. 4 and 5 for a different Oldroyd-B jet. It is evident that secondary filaments are created at the necks by the stretching that follows the recoil of the primary filament. The bead is unaffected during the recoil and the secondary filament joins it at a neck that is quite similar to the neck of the primary filament. However, the secondary filament is much thinner than the primary one and, as shown in Fig. 4(b), has a much larger elastic stress. The simulated elastic stress evolution shows that the stress actually drops at the primary neck before forming a sharp maximum due to the stretching that creates the secondary filament. This suggests the recoil of the pri-
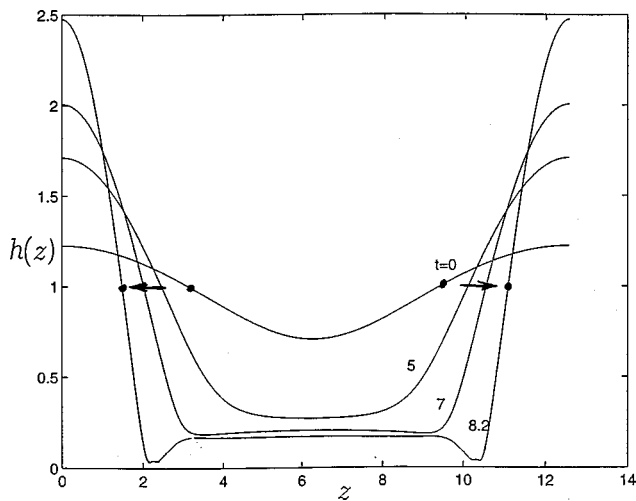


FIG. 2. Evolution of a highly elastic Oldroyd-B jet from the Rayleigh instability, to the formation of a filament by stretching and to the beginning of recoil at the necks of the draining filament. The nodes during the Rayleigh instability, which bound the jet interval that is stretched into a filament, are marked. ($We=10{,}000$, $S=0.25$, $Ca=10$, and $l=4\pi$).
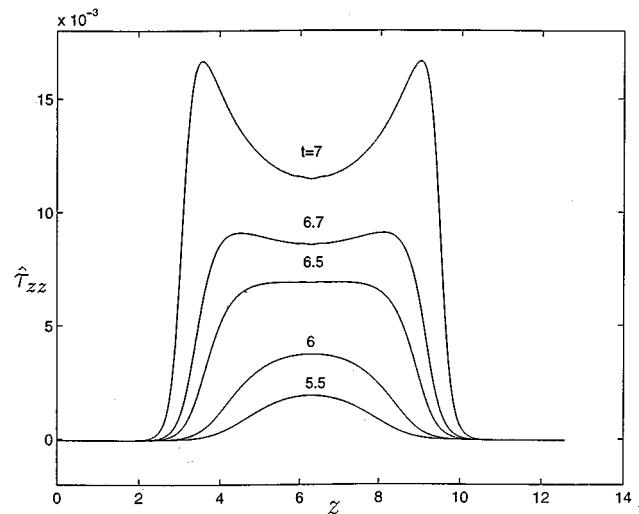


FIG. 3. The built-up of the axial elastic stress $\hat{\tau}_{zz}$ in the stretched filament of Fig. 2. The elastic stress is constant within the straight filament until recoil at the necks triggers two sharp maxima.
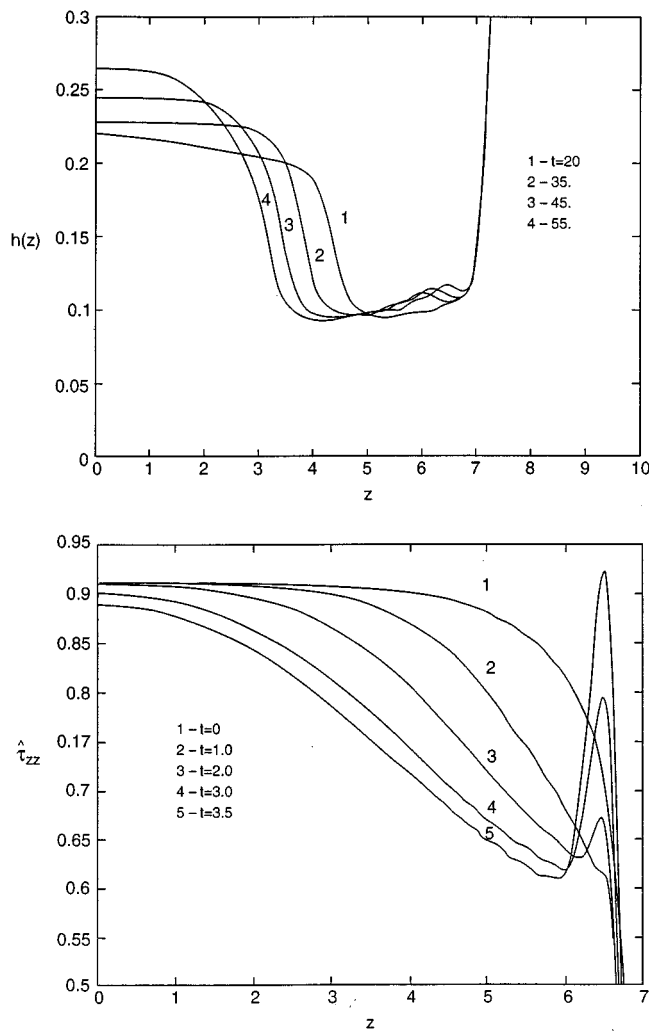
FIG. 4. Blow ups of the Oldroyd-B interface recoil and elastic stress evolution at one of the necks. For clarity, snapshots at different time, measured from the onset of pinching at the bottom figure, are taken in the two plots. Note that the elastic stress is first relieved at the neck before the sharp maximum develops due to secondary stretching. ($We=300$, $S=0.25$, $Ca=10$, and $l=4\pi$).



FIG. 5. The entire jet profiles before and after the recoil of the Oldroyd-B jet in Fig. 4. A secondary filament is clearly visible.

mary filament is triggered by a relief of the tension at the neck. The fully formed secondary filament, in the presence of the bead and the primary filament, is shown in Fig. 5.

We are unable to numerically track the jet dynamics after the formation of the secondary filament. However, since its neck with the bead is quite similar to that of the primary one, we expect another recoil to initiate there. Iterated recoil and stretching dynamics can then proceed indefinitely at the necks of Oldroyd-B jets. In our subsequent analysis, we shall develop a theory for Oldroyd-B filaments and show that their similarity allows us to relate their radii and elastic stress. As a result, with proper scalings of $We$, $Ca$, and $S$, the evolution and recoil of the primary filament can be used to deduce those of higher-generation filaments. We shall also demonstrate preliminary experimental evidence of this self-similar iterated stretching dynamics.

The evolution of the Oldroyd-B jet radius, the axial stress $\hat{\tau}_{zz}$ and the velocity $u_{max}$ at the neck of the first filament are shown in Fig. 6. There are two distinct slow stages
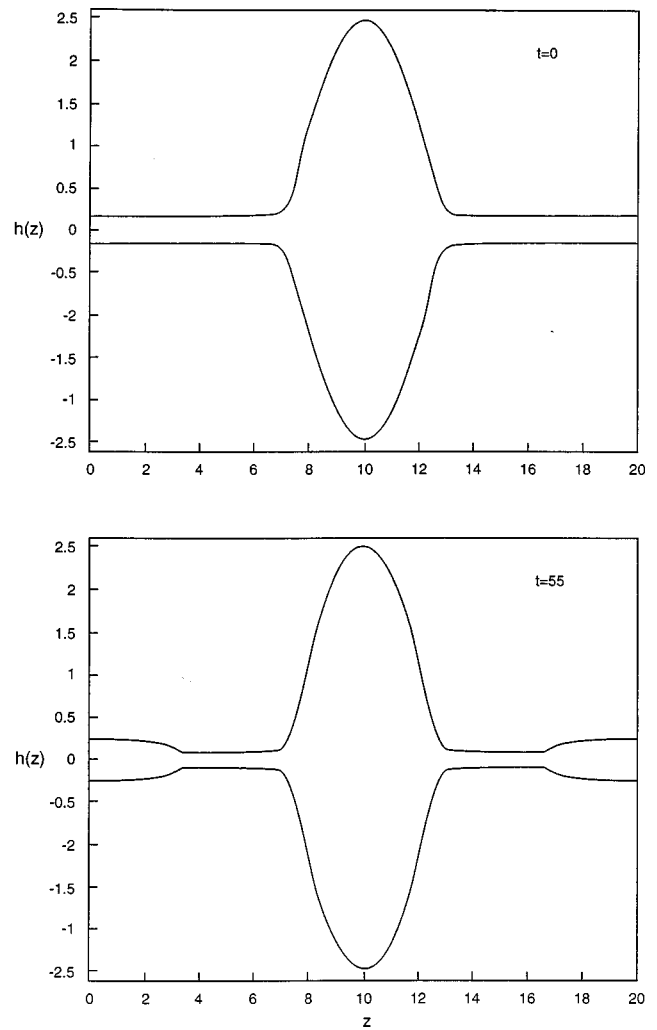
prior to the first pinch recoil that define the lifetime of the primary filament. The jet radius drops and the axial stress rises precipitously during the stretching stage near $t=100$ to form the constant-radius filament. The profiles shown in Fig. 7 indicate the transformation to an axisymmetric filament with a constant stress and a linear axial velocity profile that reaches $\pm u_{max}$ at the necks. However, this stretching stage ends abruptly as $u_{max}$ approaches zero and both filament radius and its stress reach constant values. An even slower elastic drainage then takes over after a short transient for $t>100$. The radius continues to decrease and the stress continues to increase within the filament after this short hesitation, but at distinctly slower rates than the stretching interval. The maximum axial velocity at the necks, however, remains constant during this long interval. Due to the linear uniaxial flow, this implies the strain rate in the filament remains constant during this interval.

In Fig. 8, the evolution of jet radius at the first neck is shown for a large range of $We$ and $Ca$ for an Oldroyd-B fluid. The stretching, drainage and recoil stages show appreciable sensitivity to these values.

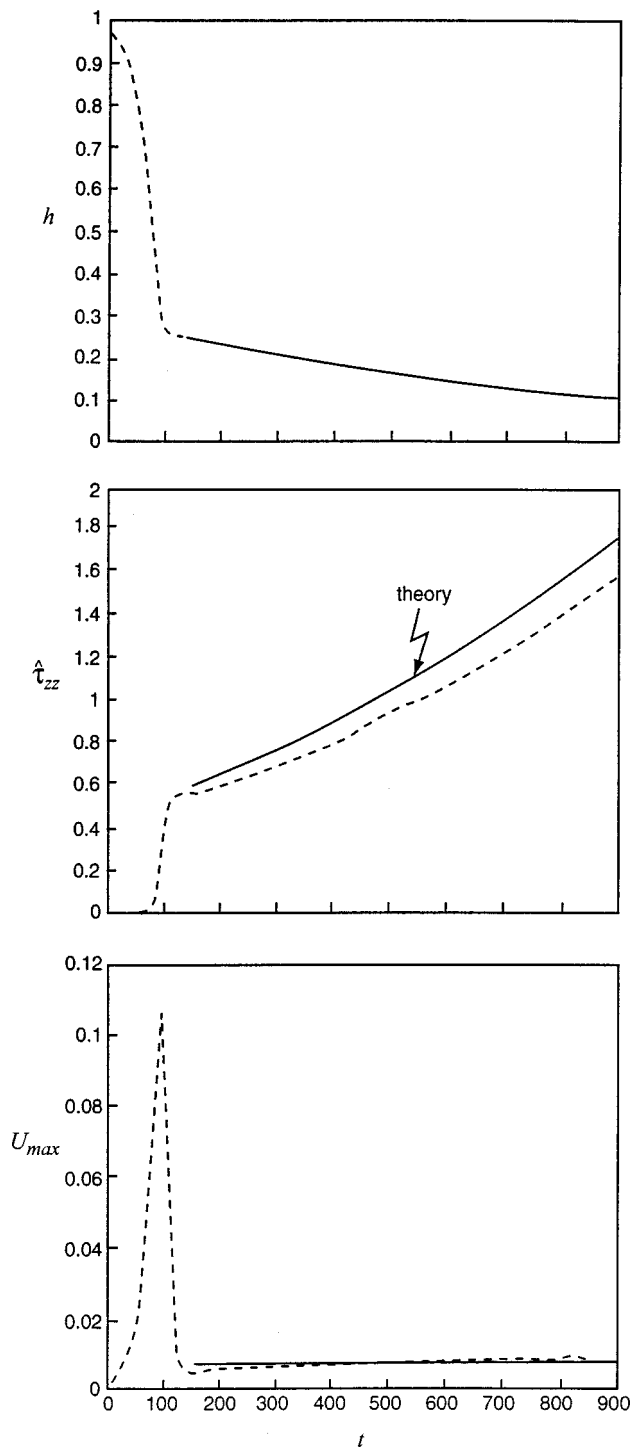We examine the dynamics of the FENE jet in Fig. 9 as a

FIG. 6. Evolution of the jet (filament) radius, elastic stress (measured at the middle of the filament), and strain-rate (maximum axial velocity at the neck) of an Oldroyd-B jet (filament) prior to recoil. Theoretical predictions are also shown. ($We=300$, $S=0.25$, $Ca=10$, and $l=20$).

function of extensibility $L$. The formation dynamics of the primary filament and the subsequent elastic drainage dynamics are insensitive to $L$ for $L$ in excess of 10. This suggests that the stretching $A+B$, is much smaller then $L^2$ in both the initial jet and the primary filament under such conditions. However, the recoil dynamics in Figs. 3 and 4 suggest that the secondary filament formed after the recoil will have a much higher axial elastic stress and hence high $A+B$ is ex-

pected. Correspondingly, the low-$L$ evolution in Fig. 9 may well represent the dynamics of higher-generation filaments. This will be further verified by an analysis that relates the recoil dynamics of filaments of different generation.

As seen in Fig. 9, the low-$L$ primary filament drains much faster than the highly extensible filaments. In fact, it does not recoil at the neck and seems to pinch off in finite time. Entov and Hinch[12] have predicted this outcome for a constant-radius filament. An insert of the low-$L$ filament-bead profile immediately before pinch off is shown in the insert of Fig. 9. Instead of a recoil, the straight filament remains during the final precipitous drop in $h(t)$ of Fig. 9. A much thinner filament drains rapidly at this stage and remains stable to the instabilities that trigger recoil. This then suggests that iterated stretching will eventually stop when $A+B$, the stretching, is the same order as $L$ for high-generation filaments.

Our analysis to establish the self-similarity of filaments of different generation begins with the linear Rayleigh instability and the ''hyperbolic'' stretching it creates that forms the primary filament. This formation dynamics can then be used to fully specify the slow exponential elastic draining dynamics for the Oldryod-B jet shown in Fig. 6. The instability that triggers the recoil at the neck is then scrutinized. In contrast to the Rayleigh instability that creates the primary filament, the resulting recoil begins with Egger's self-similar pinching with negligible elastic effect and followed by the same stretching and drainage dynamics of the primary filament. We are then able to estimate the radius and stress of the secondary filament and, by induction, relate all high-generation filaments to the previous generation. In the process, we delineate the self-similarity of all high-generation filaments until finite extensibility becomes important. When extensibility comes into play, the drainage is too rapid for the recoil instability to take effect and Fig. 9 indicates that pinch off will occur instead.

## III. LINEAR STABILITY THEORY AND ONSET OF STRETCHING DYNAMICS

We shall examine jets with large $We$ and $L$. As seen in Fig. 9, the initial instability, the filament formation dynamics and the drainage dynamics are insensitive to $L$ as long as it is in excess of 10. We hence focus only on the Oldroyd-B jet here. The stretching dynamics will be shown to be described by a coupled set of hyperbolic equations and, as such, its evolution has a strong memory that remembers the initial condition and evolution. Fortunately, the initial evolution involves small-amplitude deviations from the initial jet and can be captured by a standard linear analysis that is further simplified by our longwave expansion. Consider a standard normal mode perturbation of the straight jet basic state

$$\begin{pmatrix} h \\ u \\ \hat{\tau}_{zz} \\ \hat{\tau}_{rr} \end{pmatrix} \sim \begin{pmatrix} 1 \\ 0 \\ 0 \\ 0 \end{pmatrix} + \begin{pmatrix} h' \\ u' \\ \tau'_{zz} \\ \tau'_{rr} \end{pmatrix} e^{i\alpha z + \lambda t}. \tag{13}$$
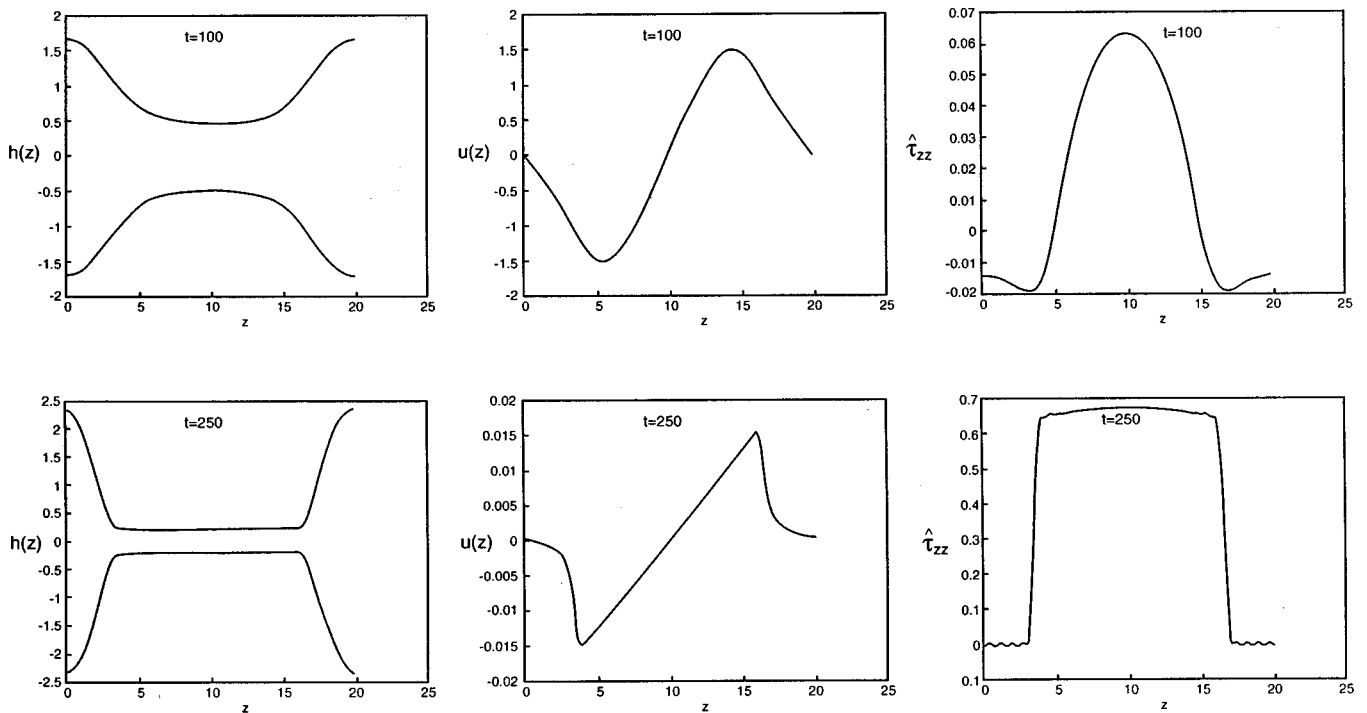
FIG. 7. Radius, velocity, and stress profiles of Fig. 6 at various times during the filament formation and drainage stages.

In the limit of large $We$, one obtains the following relationships between the stresses and the deviation radius from the linearized versions of Eqs. (9) and (11)

$$\tau'_{zz} = -\frac{2i\alpha(S-1)}{We}u' = -\frac{4(1-S)}{We}h', \tag{14}$$

$$\tau'_{rr} = \frac{i\alpha(S-1)}{\lambda We}u' = \frac{2(1-S)}{We}h'. \tag{15}$$

The growth rate $\lambda$ is determined from the dispersion relationship

$$2We\lambda^3 + (2+6\alpha^2 SWe)\lambda^2 + \alpha^2\left[6 - \frac{We}{Ca}(1-\alpha^2)\right]\lambda$$

$$-\frac{\alpha^2(1-\alpha^2)}{Ca} = 0. \tag{16}$$

The simplest limit is that of a Newtonian jet ($We=0$) and it yields the classical longwave quadratic growth rate which vanishes at $\alpha=0$ and at the neutral wave number $\alpha_0 = 1$. Its maximum growth rate and wave number are

$$\lambda_{\max}^{\text{Newt}} = \frac{1}{2\sqrt{2Ca}(1+3\sqrt{Ca/2})}$$

and

$$\alpha_{\max}^{\text{Newt}} = \frac{1}{\sqrt{2}(1+3\sqrt{Ca/2})^{1/2}}. \tag{17}$$

In the limit of large $We$, the elastic effect becomes negligible—the relaxation time approaches infinity. This corresponds to a zero eigenvalue which can be factored out of

the cubic polynomial [Eq. (16)]. The resulting quadratic corresponds to a longwave growth rate with a neutral mode at $\alpha_0 = 1$ and a maximum-growing mode with

$$\lambda_{\max} = \frac{1}{2\sqrt{2Ca}(1+3S\sqrt{Ca/2})}$$

and

$$\alpha_{\max} = \frac{1}{\sqrt{2}[1+3S\sqrt{Ca/2}]^{1/2}}. \tag{18}$$

The extra mode whose growth rate vanishes at $We\to\infty$ can be determined by standard expansion to be stable

$$\lambda_3 \sim -\frac{1}{We}\left(1 + \frac{6Ca}{We(1-\alpha^2)} + \cdots\right). \tag{19}$$

These results are consistent with earlier linear stability analysis of the full equations for the Oldroyd-B jet, the Maxwell jet ($S=0$) at large $We$, and the Newtonian jet at $We=0$.[8,9] Since the retardation number must be less than unity, highly elastic jets yield slightly longer waves and slightly larger growth rates than Newtonian jets, as seen from Eqs. (17) and (18). The limiting Maxwell jet is the most unstable with the longest disturbances. Nevertheless, elasticity has little effect in the initial evolution.

Despite the negligibly small elastic stresses, we are able to decipher its creation mechanism at inception from this linear theory. The phase difference between $h'$ and $u'$ in Eq. (14), $h' \sim -(i\alpha/2\lambda)u'$, implies that a node in $u$ with a positive slope appears at the minimum in $h=1+h'$. This corresponds locally to an axisymmetric extensional flow with a
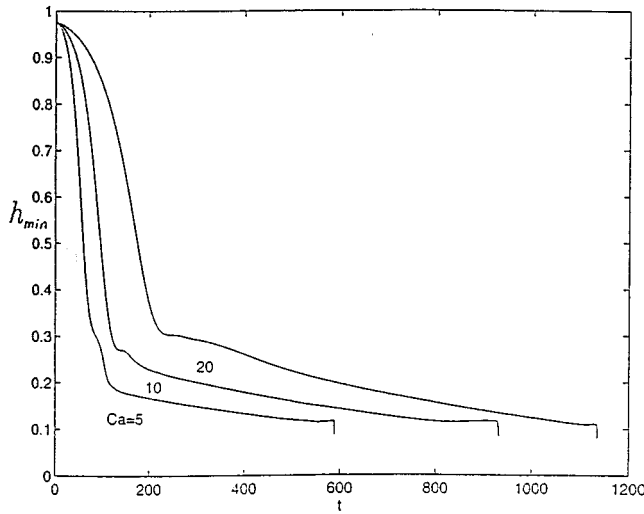
stagnation point at the jet minimum. The next relationship (15) indicates $\tau'_{zz}$ and $\tau'_{rr}$ are in phase with $-h'$ and $h'$, respectively. This reflects the result that the uniaxial extensional flow at the stagnation point has stretched the polymers and induces a maximum in $\tau_{zz}$ and a minimum in $\tau_{rr}$ at the stagnation point in the middle of the computation domain

$$\hat{\tau}_{zz} + \frac{1-S}{We} \sim \frac{(1-S)}{We}(1-4h') \sim \frac{(1-S)}{We(1+h')^4} \sim \frac{(1-S)}{Weh^4},$$
(20a)

$$\hat{\tau}_{rr} + \frac{1-S}{We} \sim \frac{(1-S)}{We}h^2,$$
(20b)

during the initial evolution with small-amplitude waves. This set of invariance between the stresses and the jet radius is the relationship that will be propagated along the characteristics during the hyperbolic stretching stage.

## IV. FILAMENT FORMATION BY STRETCHING

The axisymmetric extensional flow revealed in the linear analysis will trigger a stretching evolution that enlarges the small region near the jet minimum, with a locally constant radius, a linear axial velocity and a constant positive $\hat{\tau}_{zz}$, until a straight filament is formed. There are, of course, two additional converging stagnation points at the two jet maxima bounding the extensional stagnation point at the minimum. These regions will be compressed into beads. Hence, the stretching of the filament at the minima is accompanied by compression at the maxima. We shall focus only on the extensional flow near the minima and consequently only on filament stretching.

The scalings from the linear theory in Eqs. (14), (15), and (20) suggest that $\hat{\tau}_{zz}$ and $\hat{\tau}_{rr}$ at the above stagnation point are a factor of $We^{-1}$ smaller than $h$ and $(\partial u/\partial z)$, which are of unit order, in the stretching evolution that follows. This is consistent with our numerical results in Fig. 6.
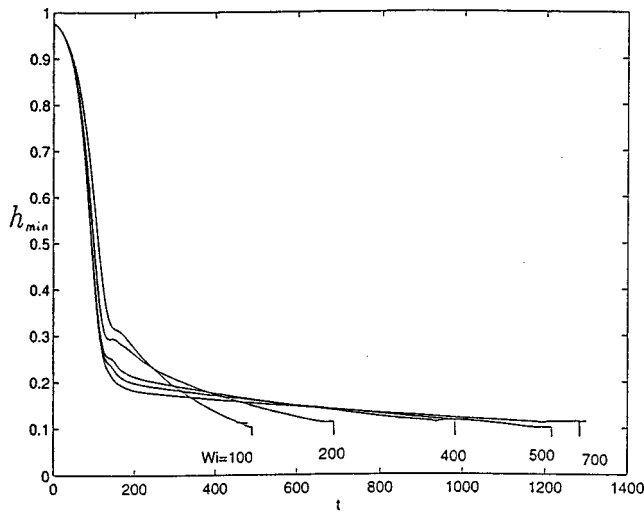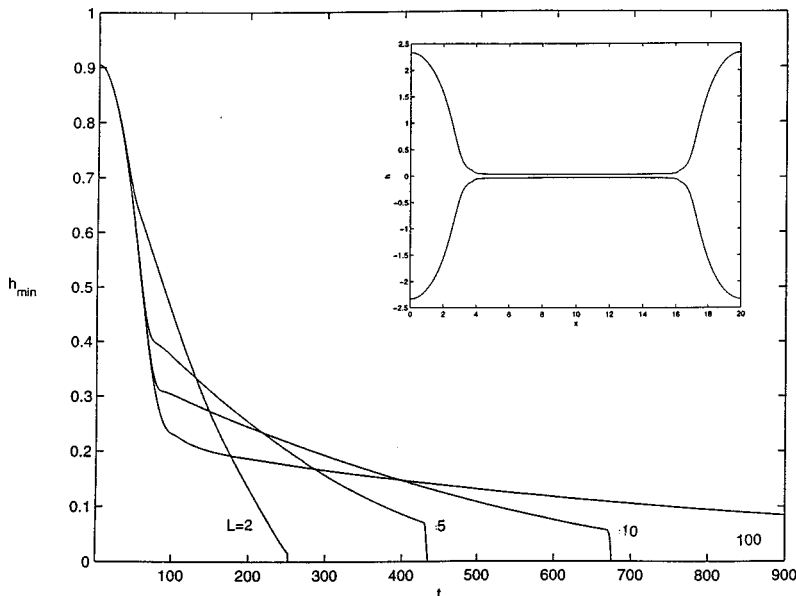


FIG. 8. Evolution of the neck radius of an Oldroyd-B jet for $S=0.25$ and $l=20$ but for the indicated ranges of $We$ and $Ca$. All exhibit the stretching, drainage, and recoil stages.



FIG. 9. The effect of extensibility $L$ on the jet evolution for a FENE jet ($We=300$, $S=0.25$, $Ca=10$, and $l=20$). There is little sensitivity to $L$ until $L>10$. The insert is the filament-bead profile at $t=243$ for $L=2$.

Also, anticipating the length of stretching stage to be governed mostly by the slow extension flow near the slender jet minimum at the stagnation point, we expect fluid inertia to be negligible in the stretching filament and the curvature $\kappa$ in Eq. (12) to be well approximated by the azimuthal curvature only, $\kappa = -1/h$.

Hence, the dominant terms in Eqs. (9) and (11) during the filament stretching stage are

$$\frac{1}{h^2} \frac{\partial}{\partial z} \left( \frac{h}{Ca} + h^2(\hat{\tau}_{zz} - \hat{\tau}_{rr}) + 3Sh^2 \frac{\partial u}{\partial z} \right) = 0, \tag{21a}$$

$$\left( \frac{\partial}{\partial t} + u \frac{\partial}{\partial z} \right) h^2 = -\frac{\partial u}{\partial z} h^2, \tag{21b}$$

$$\left( \frac{\partial}{\partial t} + u \frac{\partial}{\partial z} \right) \hat{\tau}_{zz} = 2 \frac{\partial u}{\partial z} \left( \hat{\tau}_{zz} + \frac{1-S}{We} \right), \tag{21c}$$

$$\left( \frac{\partial}{\partial t} + u \frac{\partial}{\partial z} \right) \hat{\tau}_{rr} = -\frac{\partial u}{\partial z} \left( \hat{\tau}_{zz} + \frac{1-S}{We} \right). \tag{21d}$$

The hyperbolic nature of the kinematic and stress equations in Eqs. (21b)–(21d) is quite apparent. It originates from the fact that both the liquid mass and the polymers are convected by the nearly $r$-independent axial velocity. Hence, the evolution of $h^2$, $\hat{\tau}_{zz}$, and $\hat{\tau}_{rr}$ are along characteristic lines defined by

$$\frac{dx}{dt} = u, \tag{22}$$

on which they behave as

$$\frac{dh^2}{dt} = -\frac{\partial u}{\partial z} h^2, \tag{23a}$$

$$\frac{d}{dt} \hat{\tau}_{zz} = 2 \frac{\partial u}{\partial z} \left( \hat{\tau}_{zz} + \frac{1-S}{We} \right), \tag{23b}$$

$$\frac{d}{dt} \hat{\tau}_{rr} = -\frac{\partial u}{\partial z} \left( \hat{\tau}_{rr} + \frac{1-S}{We} \right). \tag{23c}$$

Since the equation of motion [Eq. (21a)] becomes a steady force balance among capillary, elastic and viscous forces, a simple integration yields a $z$-independent force $f(t)$ that can only be a function of time

$$\frac{h}{Ca} + h^2(\hat{\tau}_{zz} - \hat{\tau}_{rr}) + 3Sh^2 \frac{\partial u}{\partial z} = f(t). \tag{24}$$

This quasi-steady balance then yields how the local flow (actually flow gradient) is determined by the local azimuthal capillary pressure and elastic stress difference.

The force $f(t)$ evolves in time during the stretching interval between the small-amplitude evolution described in the last section and the slow elastic drainage of next section. During this interval (around $\tau \sim 100$ in Figs. 6 and 8), $\hat{\tau}_{zz}$ increases dramatically and $u$ drops precipitously while the jet evolves into a filament with constant radius. We are unable to obtain the force evolution $f(t)$ explicitly but our numerical results in Fig. 10(a) indicate that it does not vary much during this stretching interval. During the small-amplitude evolution initially, the elastic stresses of Eq. (20) are small at
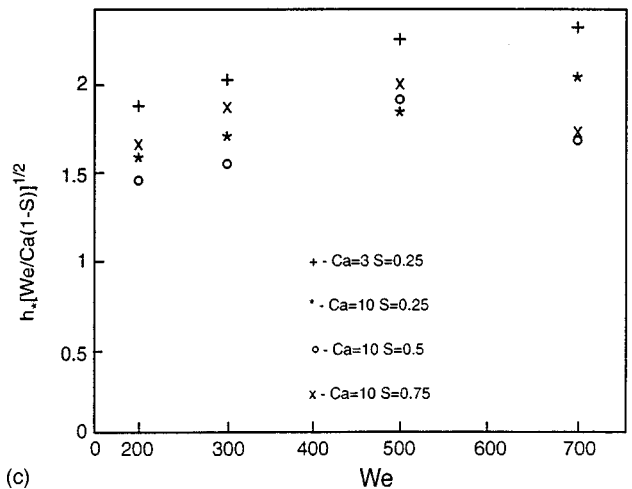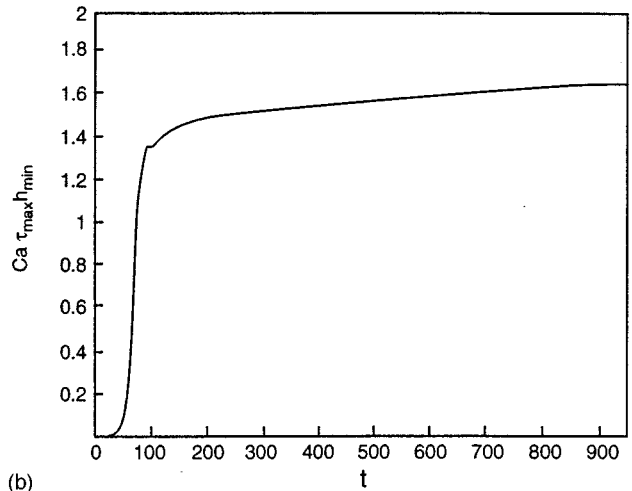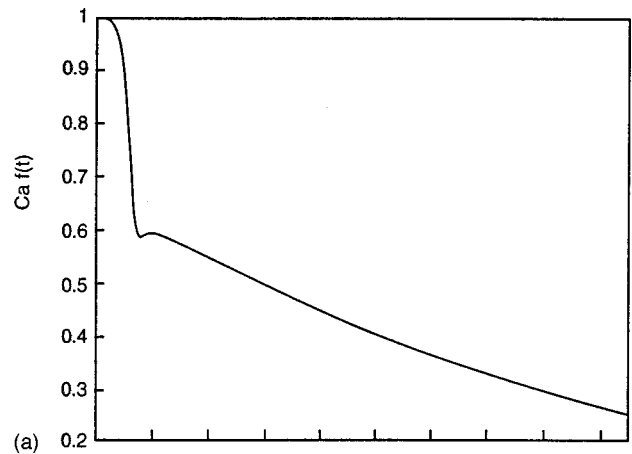


FIG. 10. (a) Evolution of the force $f(t)$ at the jet minimum in Eq. (24) showing a decrease from $1/Ca$ to $0.6/Ca$ during the stretching interval at $0 < t < 70$ for the same Oldroyd-B jet of Fig. 6. (b) Simulated value of $Cah\hat{\tau}_{zz}$ for the Oldroyd-B jet of Fig. 6, showing convergence to an asymptotic value 1.6 close to the estimated value 2 during the elastic drainage stage for $t > 100$. (c) Comparison of the simulated jet radius $h_*$ at the end of the stretching interval to estimate Eq. (30).

$O(We^{-1})$ and the axial velocity $u$ and its gradient ($\partial u/\partial z$) are both small at the order of the perturbation radius $h'$ from the original straight filament of unit radius. As a result, the initial value of the force during the stretching interval is

$$f(t) \sim \frac{1}{Ca}. \tag{25}$$

We shall use this value throughout the entire interval—the force is assumed to be also time independent. A more rigorous treatment would be to expand the evolution in both $We^{-1}$ and $t$ to discern the full evolution $f(t)$. This would be a tedious endeavor and we will numerically verify that Eq. (25) is a valid approximation. With this estimate, the quasi-steady force balance becomes

$$3S \frac{\partial u}{\partial z} = \frac{1}{Ca} \frac{(1-h)}{h^2} - (\hat{\tau}_{zz} - \hat{\tau}_{rr}), \tag{26}$$

that is valid at every point within the stretched filament. The capillary pressure and normal stress difference are balanced by polymer viscous dissipation.

We now focus on the jet minimum with a stagnation point ($u=0$). Its vanishing axial velocity implies that the corresponding characteristics line is vertical in the $t$-$x$ plane while neighboring characteristic lines diverge from it. As a result, the linear axisymmetric extensional flow region is expanded throughout the region bounded by the jet nodes. Moreover, a simple analysis of Eqs. (23a) and (23c) reveals the following invariance along the characteristics during filament stretching:

$$\left( \hat{\tau}_{zz} + \frac{1-S}{We} \right) h^4 = const_1$$

and $\tag{27}$

$$\left( \hat{\tau}_{rr} + \frac{1-S}{We} \right) h^{-2} = const_2.$$

Hence, applying this to the characteristic at the stagnation point of the jet minimum where the initial condition is provided by Eq. (20) after the small-amplitude evolution, one obtains

$$\hat{\tau}_{zz} - \hat{\tau}_{rr} = \left( \frac{1-S}{We} \right) \left( \frac{1}{h^4} - h^2 \right), \tag{28}$$

at the stagnation point.

Hence, at this minimum where $(\partial u / \partial z) > 0$, $h$ and $\hat{\tau}_{rr}$ decrease monotonically while $\hat{\tau}_{zz}$ increases monotonically as the filament is stretched. Combining Eqs. (23a), (26), and (28), we acquire the thinning rate at the minimum

$$6S \frac{dh}{dt} = -\frac{1}{Ca} \frac{1-h}{h} + \frac{(1-S)}{We} \left( \frac{1}{h^3} - h^3 \right), \tag{29}$$

where the right side represents the flow gradient between the jet minimum and the jet node as driven by the azimuthal curvature difference and retarded by the elastic stresses at the minimum. This stretching ceases when the capillary pressure increases sufficiently as $h$ decreases to balance the elastic stress in Eq. (29). This occurs when the thinning jet radius $h$ approaches

$$h_* = \left[ \frac{Ca(1-S)}{We} \right]^{1/2}, \tag{30}$$

when $\partial u / \partial z$ and $u$ approach zero as seen in Fig. 6. Physically, the elastic stress, which scales as $[(1-S)/We]h^{-4}$, as seen in Eq. (20), has reached such a high value within the filament that the liquid cannot continue to drain towards the node due to the gradient in the azimuthal curvature, which scales only as $(1/Ca)h^{-2}$. That the stretched filament reached an intermediate asymptote with constant radius is evident in all simulations seen in Fig. 8. An ''inflection point'' when the evolution ''hesitates'' is seen after the rapid decrease during the stretching stage and before the slow elastic drainage stage. The precipitous drop in the strain rate at this intermediate stage between stretching and drainage is also evident in the velocity evolution depicted in Figs. 6 and 7.

Despite the approximation made on $f(t)$ in Eq. (25), Eq. (30) is seen in Fig. 10(b) to be in good agreement with the simulated filament radius at the inflection point, prior to the slow elastic drainage stage, for a wide range of conditions. Some scatter is observed but the measured values are mostly bounded between $h_*$ and $2h_*$.

Note that this intermediate stretching interval only exists when $S$ is not zero or unity. Since we have carried out an expansion in $We^{-1}$, $S$, and $1-S$ must actually be larger than $We^{-1}$. When polymer retardation is absent ($S=0$), the quasi-steady force balance cannot be assumed and slow drainage described by Eq. (29) breaks down. The singular limit of $S=1$ corresponds to the coincidence of polymer relaxation and retardation times. At this condition, the excess elastic stresses are never triggered and the azimuthal pressure gradient drives the jet to pinch off without stretching, as in Papageorgiou's viscous jet breakup.

## V. ELASTIC DRAINAGE

At the end of the stretching interval, the filament radius has reached a small constant value $h_* \sim O(We^{-1/2})$, the radial stress $\hat{\tau}_{rr}$ remains small but the axial stress $\hat{\tau}_{zz}$ is large at $O(h_*^{-4}/We) \sim O(We)$ by Eq. (27) and the strain rate ($\partial u / \partial z$) has dropped from unit order at the beginning of stretching to negligibly small values by Eq. (26) such that there is no flow out of the filament due to stretching. However, at this point, the bead-filament configuration is established and a new capillary driving force between the filament and the bead replaces that of the initial jet in Eq. (25) during stretching. This different driving force changes the quasi-steady force balance and the magnitude of $\hat{\tau}_{zz}$. It also permits a small but finite drainage from the filament to the bounding beads. This is the elastic drainage stage that follows the stretching stage.

Instead of carrying out detailed matched asymptotics to match these two stages, we adopt a lead-order ''patching'' scheme to resolve the relaxation dynamics during this slowest intermediate drainage stage. We begin by determining the proper scalings. During this interval, the filament has already been stretched to a jet with a uniform radius $h(t)$ of order $We^{-1/2}$ as stipulated by Eq. (28). For relaxation to be included in the stress dynamics as the polymer is being stretched, $We^{-1}\hat{\tau}_{zz}$, $(\partial\hat{\tau}_{zz}/\partial t)$, and $(\partial u/\partial z)\hat{\tau}_{zz}$ must all balance in Eq. (11a). Since the filament length is unit order, $z$

$\sim O(1)$ and this yields the scaling $u \sim O(We^{-1})$ and $t \sim O(We)$ for the draining filament. Relaxation must be included to effect the pull of the stretched polymers and counter the capillary driving force such that a slow drainage into the beads can now proceed. This slow drainage is the longest process in the jet dynamics and its duration is a good estimate of the drainage time. The remaining unknown scaling is for $\hat{\tau}_{zz}$ which will be determined through a quasi-steady force and mass balance at the neck.

Once the straight filament is formed, the hyperbolic nature of the evolution is lost. During the stretching stage, the dynamics on each characteristic line are not affected by the evolution on the other characteristics. However, with the establishment of a straight filament, the linear uniaxial extension flow permeates the entire filament and the drainage dynamics over the entire filament is in unison. The driving force has also changed. During the stretching stage, there is a quasi-steady force balance governed by Eq. (24) which stipulates that the stretching flow is driven by the local azimuthal pressure gradient and countered by local elastic stress gradient and viscous dissipation. When a straight filament is formed, Eq. (25) becomes invalid as there is zero local gradient within the filament. The driving force for drainage is now provided by the azimuthal pressure drop across the neck joining the filament to the bead. To quantify this driving capillary force, a more detailed order assignment at the neck region is required. This analysis of the quasi-steady neck is absent in earlier slender filament theories.

In lieu of the quasi-steady, slender jet force balance that yields Eq. (24), we return to Eq. (9a) with the full curvature $\kappa$. Within the neck, $\kappa$ varies from $h^{-1} \sim We^{1/2}$ at the filament to $O(1)$ at the bead. We shall hence assign it the higher $We^{1/2}$ order in our dominant balance as it corresponds to the capillary pressure difference across the neck. Using the scaling $u \sim O(We^{-1})$, $t \sim O(We)$, $\kappa \sim O(We^{1/2})$ and still an unknown scaling for $z$, the width of the small neck region, we can already conclude from Eq. (9a) that the inertial terms on the left are negligible compared to the curvature gradient $(1/Ca)(\partial \kappa / \partial z)$, regardless of the scaling of $z$. This leaves the stress gradient with mostly $\hat{\tau}_{zz}$ contribution and the polymer viscous dissipation on the right for possible dominant balance with the curvature gradient. Each or both can balance the curvature gradient since both the elastic stress and viscous dissipation serve to reduce the flow from the filament to the bead while the curvature gradient drives it. We hence first seek the scalings for $\hat{\tau}_{zz}$ and $z$ when all three terms balance. This is possible when $\hat{\tau}_{zz} \sim h^{-1} \sim O(We^{1/2})$ to balance capillary pressure and elastic stress and $z \sim O(We^{-3/2})$ to balance viscous dissipation to the earlier two.

Since the neck width decreases in time as fluid is drained into the bead, the scaling $z \sim O(We^{-3/2})$ to match viscous dissipation to capillary pressure is not established initially. As the neck width decreases with drainage, viscous dissipation increases. However, the initial width is larger at say $z \sim O(We^{-1/4})$, to ensure the longwave approximation $O(h) \ll O(z)$ remains valid, and elastic stress balances capillary pressure at the neck.

Using the scalings $h \sim O(We^{-1/2})$, $\hat{\tau}_{zz} \sim O(We^{1/2})$, $z$

$\sim O(We^{-1/4})$, $u \sim O(We^{-1})$, and $t \sim O(We)$ from the above scaling arguments, we obtain the following equations for the neck region from Eqs. (9) and (11)

$$\frac{1}{Ca}\frac{\partial \kappa}{\partial z} + \frac{1}{h^2}\frac{\partial}{\partial z}(h^2 \hat{\tau}_{zz}) = 0, \tag{31a}$$

$$\frac{\partial}{\partial z}(uh^2) = 0, \tag{31b}$$

$$u\frac{\partial}{\partial z}\hat{\tau}_{zz} - 2\frac{\partial u}{\partial z}\hat{\tau}_{zz} = 0, \tag{31c}$$

where we have omitted the negligible $\hat{\tau}_{rr}$ at the end of the stretching stage. As long as the longwave approximation remains valid in the neck such that the neck width does not exceed $O(We^{-1/2})$, the radial stress remains negligible during the drainage stage and all subsequent dynamics. Due to the relatively small width of the neck compared to the filament, the force and mass balances are both quasi-steady. Simple integration of Eqs. (31b) and (31c) from the end of the filament, where the linear extensional axial velocity reaches its maximum value $u_0$ and where the filament radius and elastic stress retain the same values throughout the straight filament at $h_0$ and $\hat{\tau}_0$, to any location within the neck, yields

$$\hat{\tau}_{zz} = \tau_0(u/u_0)^2 \quad \text{and} \quad u = u_0(h_0/h)^2. \tag{32a}$$

The filament quantities with subscript 0 actually vary with time as the drainage proceeds. However, the neck stress and velocity are slaved to them according to Eq. (32) due to the narrow width of the neck. These invariances can be combined to yield a simple relationship between the neck stress and the neck radius any where within the neck

$$\hat{\tau}_{zz} = \tau_0 h_0^4 h^{-4}, \tag{32b}$$

where $\tau_0 h_0^4$ is a slowly varying function of time only.

This invariance allows us to simplify the force balance across the neck [Eq. (31a)]. It can be converted into an integrable form by Eq. (32b)

$$\frac{1}{Ca}\frac{\partial \kappa}{\partial z} + \frac{1}{2}\frac{\partial}{\partial z}\hat{\tau}_{zz} = 0. \tag{33}$$

We now integrate Eq. (33) again but now completely across the neck from the filament to the bead. The curvature and the stress at the filament are large compared to those at the bead and neglecting the subscript 0 in Eq. (32), we obtain an important invariance between the curvature and the elastic stress of the straight filament

$$Ca\hat{\tau}_{zz} = 2. \tag{34}$$

The unique factor of 2 again arises from the force and mass balance across the neck. This predicted invariance is confirmed by our numerical simulation shown in Fig. 10(c) where an asymptotic limit of $Ca\hat{\tau}_{zz} = 1.6$ is reached soon after the stretching interval at $t = 100$. The invariance (34) is distinct from earlier drainage theories which assume a slender filament without necks. A reanalysis of Renardy's result,[11] for example, yields a constant of $\frac{1}{2}$ instead of 2 in Eq. (34).

Respecting the constant radius and linear extensional flow, the proper dimensionless variables are

$$u(z,t)=zU(t)Wi^{-1}, \quad \Theta=tWi^{-1}, \tag{35}$$

where $z$ is now $O(1)$ as we return to the filament. The fact that $\hat{\tau}_{zz}(\Theta)$ and $h(\Theta)$ are only functions of $\Theta$ and not $z$ allows us to construct the leading-order filament equation from Eqs. (9b) and (11a)

$$\frac{dh}{d\Theta}=-\frac{1}{2}hU \quad \text{and} \quad \hat{\tau}_{zz}+\frac{d}{d\Theta}\hat{\tau}_{zz}-2U\hat{\tau}_{zz}=0. \tag{36}$$

We have neglected to scale $\hat{\tau}_{zz}\sim O(We^{1/2})$ and $h\sim O(We^{-1/2})$ explicitly for simplicity.

The kinematic equation [Eq. (36)] is simply a mass balance for a straight filament while the stress equation [Eq. (36)] represents stress relaxation within the filament. They both evolve exponentially for a constant uniaxial extensional flow, as shown by earlier straight-filament theories,[11,12] $h(t)\sim\exp(-Ut/2)$ and $\hat{\tau}_{zz}(t)\sim\exp[(2U-1)t]$. However, the new force balance across the neck [Eq. (34)] stipulate they are correlated in time such that their product is a constant. This is only possible if $U=\frac{2}{3}$, the maximum filament velocity at the neck remains constant during this drainage interval! This implies that the strain-rate of the uniaxial extensional flow within the draining filament remains constant at two-thirds the rate at which the stress would relax at fixed strain. Although Entov and Hinch's straight-filament theory uses a different correlation constant between $h$ and $\hat{\tau}_{zz}$, it still captures this unique constant strain rate.[12] After inserting the initial condition $h_*$ of Eq. (30) for matching with the stretching stage, we obtain the large-time asymptotic behavior

$$u(z,t)=\frac{2}{3We}z, \tag{37a}$$

$$h(t)=h_*\exp(-t/3We), \tag{37b}$$

$$\hat{\tau}_{zz}(t)=\frac{2}{h_*Ca}\exp(t/3We), \tag{37c}$$

for the draining filament in the original variables. The uniaxial extensional flow is clearly evident but the unique feature is the correlated exponential decay of $h(t)$ and exponential growth of $\hat{\tau}_{zz}(t)$ due to matching of the filament solution to the bead. These asymptotic predictions are favorably compared to the simulated evolution in Fig. 6. Matching with the final radius of the stretching stage in Eq. (30) and the proper capture of the $\hat{\tau}_{zz}$ and $h$ correlation in Eq. (35) from the neck analysis are essential to obtain the correct description of the draining filament. They are not available in earlier slender or straight filament theories.[11,12]

In both the neck analysis of Eq. (31), which yields correlations (32) for the neck, and the derivation of the important stress-radius correlation of Eq. (34) for the filament, the beads are never explicitly included. So long as their radius is much larger than the filament, the beads do not affect the leading-order filament drainage dynamics captured in Eq. (37). This also suggests that Eq. (37) is a universal drainage dynamics valid for all Oldroyd-B filaments bounded by beads. We had used the initial jet radius $r_0$ as the character-

istic length scale but one can use the actual value of the initial jet radius $h_*$. We also expect Eq. (37) to describe the drainage of the secondary filament after the recoil in Fig. 4. However, the recoil dynamics are different from the stretching dynamics of the filament in Sec. IV since the former begins at the neck while the latter at a jet minimum. Hence, the radius of the secondary filament at the onset of drainage cannot be described by the stretching analysis of Sec. IV and will, instead, be addressed in Sec. VII. In the next section, we shall determine the instability that triggers the neck recoil by analyzing the stability of the drainage dynamics in Eq. (37). Since it describes all draining filaments except the initial jet, which is not bounded by beads, we also expect the same recoil mechanism to apply for all higher generation filaments.

## VI. STABILITY OF A FILAMENT DRAINING INTO BEADS

Due to the slow elastic drainage with time scale $3We$, one can analyze the stability of the draining filament-bead configuration at any given instant in time by linearizing Eqs. (9) and (11) about the draining state as if the jet is quasi-stationary

$$\mathbf{A}\begin{pmatrix}u'\\h'\\\tau'\end{pmatrix}=\lambda\begin{pmatrix}u'\\h'\\\tau'\end{pmatrix}, \tag{38}$$

where the differential operator $\mathbf{A}$ is

$$A_{11}=-\frac{d}{dz}(u\cdot)+\frac{3S}{h^2}\frac{d}{dz}\left(h^2\frac{d}{dz}\cdot\right),$$

$$A_{12}=\frac{1}{Ca}\left(\frac{d^3}{dz^3}\cdot+\frac{1}{h^2}\frac{d}{dz}\cdot-\frac{2}{h^3}\frac{dh}{dz}\cdot\right)-\frac{2}{h^3}\frac{d}{dz}(h^2\hat{\tau}_{zz})\cdot$$
$$-\frac{6S}{h^3}\frac{d}{dz}\left(h^2\frac{du}{dz}\right)\cdot+\frac{1}{h^2}\frac{d}{dz}(2h\hat{\tau}_{zz}\cdot)$$
$$+\frac{3S}{h^2}\frac{d}{dz}\left(2h\frac{du}{dz}\cdot\right),$$

$$A_{13}=\frac{1}{h^2}\frac{d}{dz}(h^2\cdot),$$

$$A_{21}=-\frac{1}{2h}\frac{d}{dz}(h^2\cdot),$$

$$A_{22}=-\frac{1}{h}\frac{d}{dz}(hu\cdot),$$

$$A_{23}=A_{32}=0,$$

$$A_{31}=-\frac{d}{dz}(\hat{\tau}_{zz}\cdot)+3\hat{\tau}_{zz}\left(\frac{d}{dz}\cdot\right)-\frac{2(S-1)}{We}\left(\frac{d}{dz}\cdot\right),$$

$$A_{33}=-\frac{d}{dz}(u\cdot)+3\frac{du}{dz}\cdot-\frac{1}{We}\cdot.$$

The dynamics of $\hat{\tau}_{rr}$ have been neglected due to the slenderness of the neck and $\tau'$ represents the disturbance to the excess axial elastic stress.
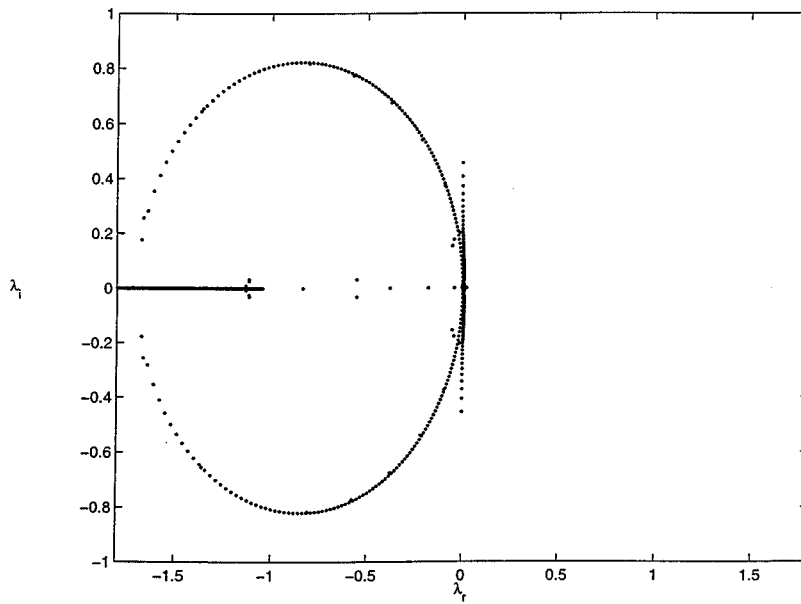
FIG. 11. The spectrum of the Oldroyd-B bead-filament configuration with a draining filament in Fig. 6 at $t = 500$. The dominant structures are the stable bands on the ellipse and the negative real axis. The fine structures near the origin are shown in Fig. 12.

Assuming the same periodicity, over the domain of length $l$, for the disturbance and the evolving jet, the computed spectrum with a spectral numerical method at $t = 500$ for the draining filament in Fig. 6 is shown in Fig. 11 with a blow-up of the origin in Fig. 12. Most of the spectrum is stable and the stable eigenvalues form a nearly continuous band of ellipse and a nearly continuous line on the negative real axis, as is evident in Fig. 11. Continuous spectrum is obviously impossible with a finite domain size $l$ but both stable bands do approach continuum as $l$ becomes large. The stable ellipse terminates on the negative real axis near the origin, as seen in Fig. 12. (Discrete eigenvalue 1 is an exten-

sion of the ellipse.) Several additional branches (2 and 3) bifurcate from the ellipse near the origin. Complex branch 3 tends to approach the imaginary axis while branch 2 extends slightly into the stable region on the negative real axis. The member of the eigenfunction corresponding to radius disturbance is also shown in Fig. 12 for some typical members of the more unstable branches 1 and 3. The disturbances of both branches are confined to the filament and decay exponentially into the beads. The disturbances of branch 3, however, also decay towards the middle of the filament.

The most unstable branch 4, however, protrudes into the left half of the complex plane on the positive real axis. At $t = 500$, the most unstable mode of this branch is at $\lambda_r \approx 0.019$ and this value is nearly constant up to $t = 1000$. Its eigenfunction is also shown in Fig. 12 which suggests that all the disturbances of this branch 4 are confined to the beads.

There are hence two classes of disturbances, one confined to the filament and one to the beads. Although the latter seems more unstable, both decay towards the neck where the recoil initiates. We can better understand why the recoil initiates at the neck with a deeper analysis of the spectral problem (38). If we omit the beads and use the estimated filament solution of Eq. (37) over an unbounded domain, the computed spectrum shown in Figs. 13 and 14 yields both the stable ellipse in Fig. 13 and branches 1, 2 and 3 near the origin in Fig. 14 at $t = 500$. Other than some details near the origin, due to mode interaction with the beads, the branches are all quantitatively reproduced. Even the eigenfunctions, including the odd branch 3, are captured correctly if one allows for the fact that they do not decay into the missing beads.

In fact, analytical expressions can be derived from Eq. (38) in the limit of infinite $We$. In this limit, the $z$-dependent uniaxial velocity profile $u(z,t)$ in Eq. (37a) vanishes and hence the coefficients of the operator $\mathbf{A}$ become constant. This allows the usual normal mode expansion to yield a simple dispersion relationship. Due to the omission of the uniaxial extensional velocity field, $\lambda = 0$ is always a solution
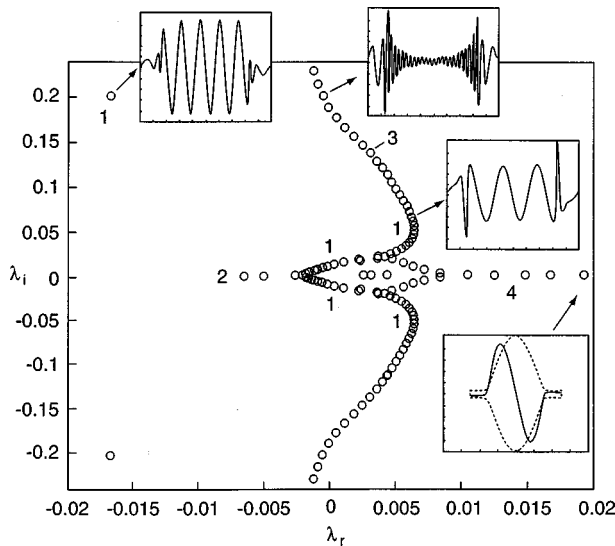


FIG. 12. Blow-up of the fine structures of the spectrum near the origin of the complex plane. The vertical branch to the right of the ellipse in Fig. 12 is branch 3 here. Mode 1 is part of the ellipse and branch 2 is a stable real branch. The most unstable branch 4 is opposite branch 2 on the positive real axis. The radius eigenfunctions of branches 1, 3, and 4 are shown in inserts. The former two are confined to the filament in the middle and decay into the beads at the two ends. The eigenfunction of branch 4 is confined to the bead in the middle of that insert.
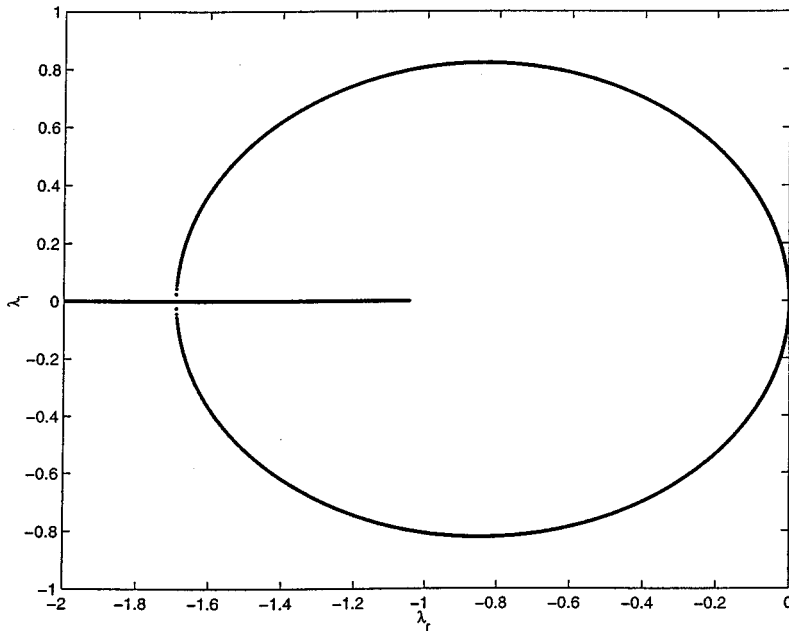
FIG. 13. Spectrum of an infinitely long draining filament. The computed values are indistinguishable from the analytical result with $h = h_* \exp(-t/3We)$ at $t = 500$.

with no velocity fluctuation $u' = 0$. Omitting this neutral mode, the other two modes are determined by the dispersion relationship

$$\lambda^2 + 3S\alpha^2\lambda - \alpha^2\left(\frac{1}{2Cah} - \hat{\tau}_{zz}\right) + \frac{\alpha^4 h}{2Ca} = 0. \tag{39}$$

Comparing this to the Rayleigh dispersion relationship for an unstretched filament of unit radius $(h-1)$ in Eq. (18), one can easily see that the positive elastic stress $\hat{\tau}_{zz}$ has a stabilizing effect.

If one further introduces the derived correlation (34) of a stretched filament under drainage into beads, the spectrum can be estimated explicitly as a function of the filament radius $h$

$$\lambda = -\frac{3}{2}S\alpha^2 \pm \sqrt{\frac{9}{4}S^2\alpha^4 + \frac{h}{2Ca}\alpha^2(1-\alpha^2) - \frac{2\alpha^2}{Cah}}. \tag{40}$$

This analytical dispersion relationship for an highly elastic $(We \rightarrow \infty)$ stretched filament quantitatively captures the stable ellipse and stable real branch of Figs. 11 and 13, if one uses the estimate (37b) for the filament radius $h(t)$ at $t = 500$.

The ellipse corresponds to small $\alpha$ and is well approximated by

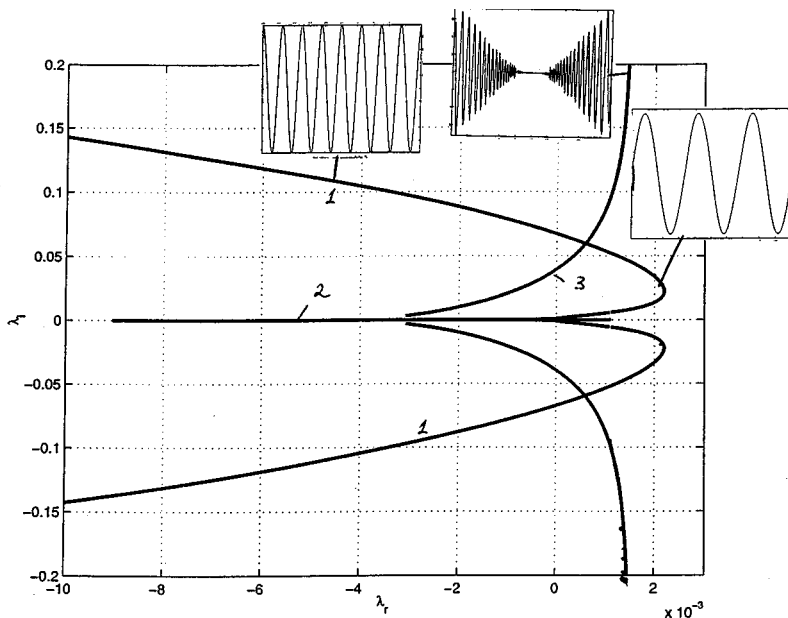$$\lambda = -\frac{3}{2}S\alpha^2 \pm i\alpha\sqrt{\frac{2}{Cah}}. \tag{41}$$



FIG. 14. The spectrum of the infinitely long draining filament near the origin and representative eigenfunctions.

Phys. Fluids, Vol. 11, No. 7, July 1999
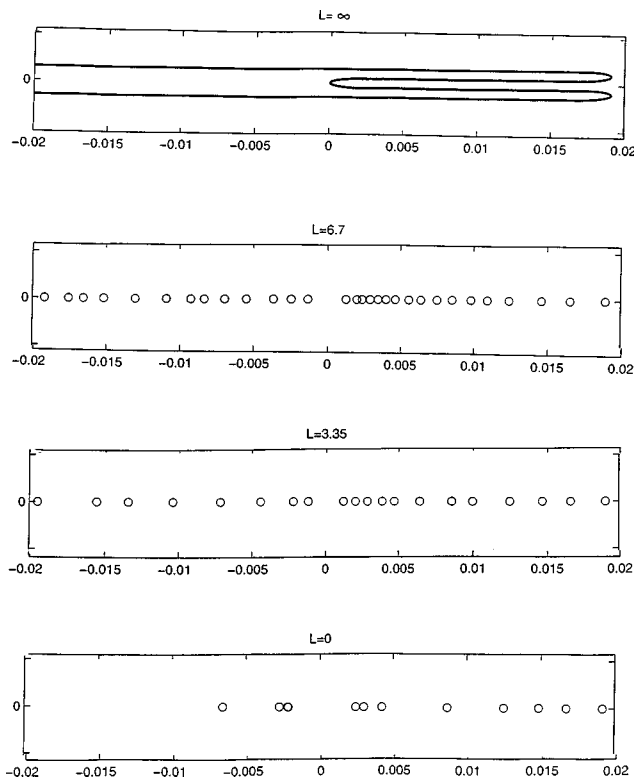
Iterated stretching of viscolelastic jets     1731



FIG. 15. The spectra of the bead with a cylindrical insert of length $L$. The $L=\infty$ limit is the Rayleigh instability and the $L=0$ limit is the bead mode of branch 4 in Fig. 12.

The stable real mode is at large $\alpha$, corresponding to $-3S\alpha^2$. Obviously, the actual filament length $l$ imposes an upper bound of $\alpha=(2\pi/l)$.

The bead branch 4 can likewise be estimated by linking it with the Rayleigh instability of a cylinder. We insert in the middle of the bead a cylinder of length $L$ and a radius identical to that of the bead. We than remove the filaments from the elongated bead such that the structure has a length roughly equal to the sum of the diameter of the original bead and $L$. The results are insensitive to the exact location where the filaments are removed. We then impose periodic boundary condition for the disturbance over this structure and solve the full eigenvalue problem with the prescribed $h$ and with negligible elastic stress $\hat{\tau}_{zz}$. At infinite $L$, we obtain the continuous Rayleigh spectrum of an infinitely long cylinder of Eq. (18), after correcting for the new cylinder radius:

$$\lambda_{\text{Rayleigh}} = -\frac{3}{2}S\alpha^2 \pm \sqrt{\frac{9}{4}S^2\alpha^4 + \frac{\alpha^2}{2Cah} - \frac{\alpha^4}{2Ca}}. \qquad (42)$$

As $L$ becomes finite, this continuous spectrum breaks up into discrete modes. But as is evident in Fig. 15, the discrete modes lie approximately at the same location as the continuous modes of Eq. (42) and approach those on branch 4 of Fig. 12 at $L=0$. Branch 4 can hence be attributed to the Rayleigh instability of a bead with openings to filaments.

The relative dominance of the unstable bead branch 4 and the unstable filament branch 1 at the neck must be determined by a different spectral theory. The continuous filament spectrum Figs. 13 and 14 and the continuous bead Ray-

leigh spectrum of Fig. 15 at $L=\infty$ correspond to normal modes in unbounded domains. However, if one introduces a generic localized disturbance, the local effect of the resulting wave packet is not determined by the spectrum $\lambda(\alpha)$ of the normal modes. Specifically, consider a generic disturbance of the form

$$h'(z,t) = \int_{-\infty}^{\infty} A(\alpha)e^{i\alpha z + \lambda(\alpha)t}d\alpha, \qquad (43)$$

where $A(\alpha)$ is the Fourier coefficient of the initial localized disturbance and the evolution in time is specified by the linearized equations of Eq. (38).

At a specific location, $z=0$ say, the dynamics (43) are dominated by a single complex mode $\alpha^*$ derivable by Wentzel–Kramers–Brillouin (WKB) theory [19]

$$\frac{d\lambda}{d\alpha}(\alpha^*) = 0, \qquad (44)$$

where $\alpha = \alpha_r + i\alpha_i$ is complex and so is $\lambda = \lambda_r + i\lambda_i$. Hence, the contribution of all modes at the neck (and any other location) is determined by the growth rate at the above saddle point $\alpha^*$ in the complex plane. An unstable spectrum in an unbounded domain is "absolutely" unstable if $\lambda_r(\alpha^*)$ is positive. Otherwise, it is convectively unstable—disturbances will connect pass the neck without triggering any local instability. The growth would then occur only in a moving frame and would not be felt at any specific location. This classification of an unstable spectrum is most pertinent to instabilities which possess a specific sensitive spot—the neck in the present example.

We determine the absolute and convective stability of both the filament and bead continuous spectra by exploiting the Cauchy–Riemann condition. Since both $\lambda$ and $\alpha$ are complex in Eq. (44), $\alpha^*$ can be determined from $(\partial\lambda_r)/(\partial\alpha_r) = (\partial\lambda_r)/(\partial\alpha_i) = 0$ only. We optimize with respect to $\alpha_r$ and $\alpha_i$ sequentially to locate the saddle point $\alpha^*$. In Fig. 16, we fix $\alpha_i$ for both the filament and bead spectra and plot the spectra $\lambda(\alpha_r + i\alpha_i)$ as parameterized by $\alpha_r$ from zero to infinity. We then seek the maximum $\lambda_r$ with respect to $\alpha_r$ on these spectra, $\lambda^{\max}(\alpha_r^{\max},\alpha_i)$. For all $\alpha_i$ in both cases, this optimum is located on the real axis, $\alpha_r^{\max}=0$. We then vary $\alpha_i$ to optimize $\lambda^{\max}$ with respect to $\alpha_i$ along the real axis. As seen in Fig. 16, the filament spectrum at $t=500$ is convectively unstable with $\alpha^*=2.2i$ and $\lambda(\alpha^*)=-0.6$ while the bead spectrum is absolutely unstable with $\alpha^*=1.15i$ and $\lambda(\alpha^*)=0.466$. The unstable filament spectrum of Fig. 14 hence does not contribute to local growth at any location, including the neck. Its growth is in a moving frame. The unstable bead spectrum of Fig. 15, on the other hand, contributes to a local growth rate of 0.466 that is far in excess of its maximum value 0.019 on the original spectrum. It is the ability of Rayleigh modes to accumulate at the neck that accounts for the absolute instability which triggers the recoil.

The same conclusion that the bead mode is absolutely unstable has also been verified at larger $t$ during the drainage interval. Although our analysis is carried out for the continu-
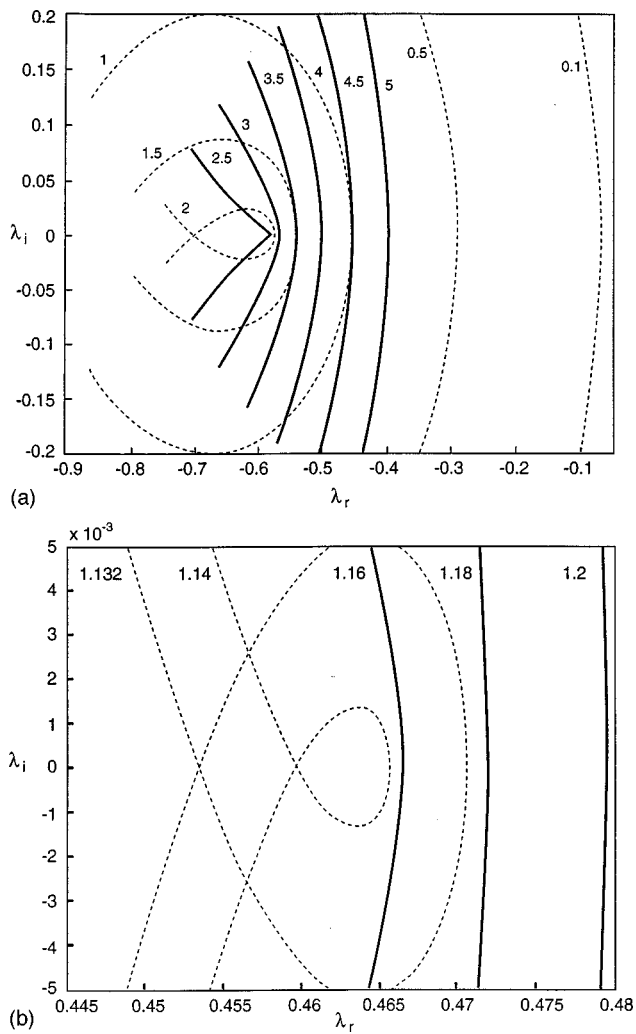
FIG. 16. The spectra $\lambda(\alpha_r + i\alpha_i)$ parameterized by $\alpha_i$. The solid spectra correspond to those whose $\lambda_r^{max}$ decrease with $\alpha_i$ and the dashed lines are those that increase. (a) The filament spectrum with $\alpha^* = 2.2i$ and $\lambda(\alpha^*) = -0.6$. (b) The bead spectrum, as approximated by the Rayleigh spectrum with $\alpha^* = 1.15i$ and $\lambda(\alpha^*) = 0.466$.

ous band at $L = \infty$, we expect the discrete modes at $L = 0$ to behave likewise due to their similarity in Fig. 15.

To verify that it is the disturbances from the bead and not the filament that trigger neck recoil, we have performed a large number of numerical simulations. If localized disturbances are placed on the draining filament, they are observed to convect pass the necks and vanish within the beads. If they are placed on the beads, they expand into the neck and quickly trigger a recoil. To show that the recoil is indeed a result of this instability, we place the same disturbance within the bead at $t = 400$, 600, and 800 in Fig. 17. Each disturbance triggers a recoil as seen in the figure. Without the disturbance, the drainage would continue undisturbed by the predicted dynamics of Eq. (37). The simulation in Fig. 17 is carried out with a FENE model with extensibility $L = 100$. It is clear that, for $L$ in excess of 10, the above recoil initiation due to absolutely unstable disturbances from the bead is independent of $L$. For smaller $L$, however, Fig. 9 indicates the filament drainage is much faster than the Oldroyd-B exponential drainage of Eq. (37). Earlier theory[12] suggests $h(t)$ decreases linearly until breakup. The linear thinning is consistent with Fig. 9 but the predicted rate does not agree with our simulation. Nevertheless, this fast thinning invalidates the quasi-steady assumption in the current filament stability analysis. From the simulations, a low-L filament seems to ''outrun'' the convective instability from the bead such that a recoil is never triggered. We are unable to determine the critical $L$ that separates unstable filaments from stable ones.

## VII. FORMATION OF HIGH-GENERATION FILAMENTS

The absolutely unstable Rayleigh disturbances from the beads relieve the tension at the necks and quickly trigger a recoil of the primary high-extensibility filament. As seen in Fig. 4, the relieved tension is almost immediately replaced by a sharp maximum in the axial elastic stress at the neck. This elastic stress grows very rapidly as the stretching cre-
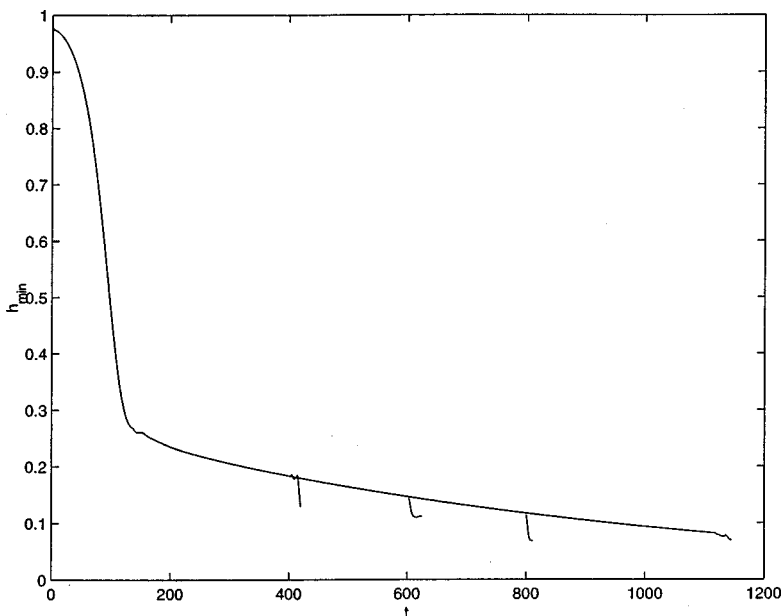


FIG. 17. Recoil triggered by small localized disturbances placed in the beads at $t = 400$, 600, and 800. This simulation was actually done with a FENE model with all conditions identical to those of Fig. 6 but with extensibility $L = 100$.
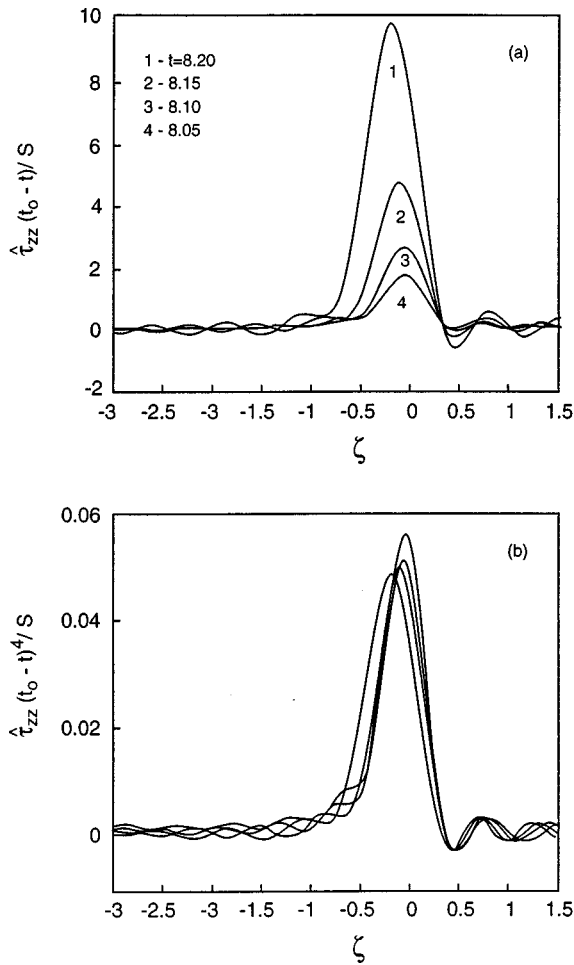
FIG. 18. Rescaling of the stress evolution near the neck beyond the recoil of Fig. 4 by (a) Newtonian pinching scaling and (b) viscoelastic pinching scaling. ($We = 10,000$, $S = 0.25$, $Ca = 10$, and $l = 12.5$.)

ates a much finer secondary filament near the neck with a much larger azimuthal curvature. The small spike in $\hat{\tau}_{zz}$ of Fig. 4 rapidly grows into a large maximum, much larger than $\hat{\tau}_{zz}$ of the primary filament, as seen in Fig. 18(a).
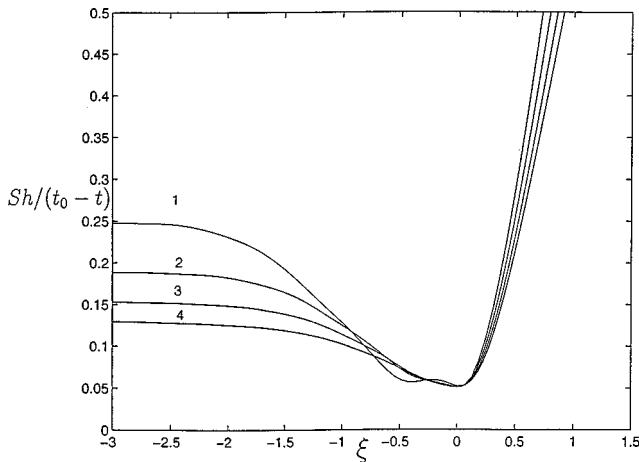


FIG. 19. Normalization of the interface evolution near the neck beyond recoil. Conditions same as those in Fig. 18.

The secondary filament formed must still obey the same quasi-steady force balance (26) and the kinematic condition (23a) of the primary filament before its drainage due to polymer relaxation. Combining these equations, we get

$$6S\frac{dh}{dt} = \hat{\tau}_{zz} - \frac{1}{Cah}, \tag{45}$$

where we have neglected $1/h$ relative to $1/h^2$ in the capillary term and have omitted $\hat{\tau}_{rr}$. We hence expect the elastic stress to again balance the azimuthal capillary pressure to form a secondary filament of radius

$$h_* = \left(\frac{1}{\hat{\tau}_{zz}Ca}\right)^{1/2}. \tag{46}$$

However, since the stretching here arises from the recoil and not the elastic stretching of the Rayleigh instability in Sec. III, we cannot use the stress-radius correlation of Eq. (28) in Eq. (46) to obtain an explicit prediction for the secondary filament radius. Instead, we need to resolve the pinching dynamics during the recoil. We shall associate such dynamics with a self-similar solution that evolves from the primary filament, after being triggered by the Rayleigh instability from the beads.

The pinching dynamics triggered by the bead disturbances push fluid rapidly from the neck into the filament and the bead. This relieves the stretching and reduces the elastic stress $\hat{\tau}_{zz}$ at the neck. As a result, inertia terms are important for the first time in the jet evolution while elastic effect is negligible at the beginning of a recoil. The recoil dynamics are hence similar to that of a Newtonian jet. However, unlike inertia pinching of a Newtonian jet,[2,3,5] the extensional flow about a newly created stagnation point near the neck again creates a large local maximum in $\hat{\tau}_{zz}$ seen in Figs. 4 and 18. This elastic stress mediates the subsequent pinching dynamics considerably. Since the neck profile is asymmetric about the minimum during pinching, asymmetric stretching occurs initially that evolves later into a straight filament, as seen in Fig. 4.

We first attempt to simplify the force balance and kinematic conditions with the Oldroyd-B model of Eq. (11) by the self-similar transform of a Newtonian jet[7]

$$\xi = \frac{x - x_0}{S^{1/2}\sqrt{t_0 - t}}, \quad \tau = \frac{t_0 - t}{S^2},$$

$$h = SH(\xi)\tau/Ca, \quad u = S^{-1/2}\tau^{-1/2}V, \tag{47}$$

$$\hat{\tau}_{zz} = \frac{X(\xi, \tau)}{S\tau}, \quad \hat{\tau}_{rr} = \frac{Y}{S\tau},$$

where $t_0$ is a nominal ''pinchoff'' time when the filament radius $h$ vanishes at $x = x_0$. Although this pinchoff is never completed due to elastic effects that form the secondary filament in Eq. (45), scaling Eq. (47) is still appropriate in an intermediate interval beyond the initiation of the recoil and before the secondary filament is established. This is quite analogous to the termination of the hyperbolic stretching stage in Eq. (23) when the jet nodes have been convected into the beads. After that, a straight filament is formed and

begins to drain by the elastic time scale $3We$, as described by Eq. (37). Unlike the self-similar pinching solutions studied earlier, the current one at the neck in Eq. (47) will eventually evolve into the beads and terminate the self-similar behavior. Nevertheless, as the hyperbolic stretching yields the initial filament radius $h_*$ in Eq. (30) prior to the drainage of the primary filament, transformation (47) yields an important intermediate pinching solution that links the recoil to the straight secondary filament.

Under transformation (47), the Oldroyd-B jet of Eqs. (9) and (11) becomes, in the limit of $\tau \to 0$

$$(V + \xi/2)\frac{dV}{d\xi} + \frac{V}{2} = \frac{1}{H^2} \left\{ \frac{dH}{d\xi} + \frac{d}{d\xi} H^2(X - Y) \right.$$
$$\left. + 3\frac{d}{d\xi} H^2 V_\xi \right\}, \tag{48a}$$

$$(V + \xi/2)\frac{dH}{d\xi} = -(V_\xi/2 - 1)H, \tag{48b}$$

$$-\tau\frac{\partial X}{\partial \tau} + \frac{1}{2}(2V + \xi)\frac{\partial X}{\partial \xi} = (2V_\xi - 1)X, \tag{48c}$$

$$-\tau\frac{\partial Y}{\partial \tau} + \frac{1}{2}(2V + \xi)\frac{\partial Y}{\partial \xi} = -(V_\xi + 1)Y. \tag{48d}$$

Without the normal stress difference, Eqs. (48a) and (48b) are just the inertial self-similar equations of motion and kinematic operation of a Newtonian jet. There are described by an ode. However, the hyperbolic nature of the stress equations must be retained to propagate the initial stress profiles. Hence, one cannot omit the $\tau(\partial/\partial \tau)$ terms in Eqs. (48c) and (48d). Otherwise, $X$ and $Y$ vanish exactly as the system has no memory of the past—it collapses into the Newtonian self-similar pinchoff. Hence, the Newtonian scaling Eq. (47) is not the self-similar transform for a viscoelastic jet.

Nevertheless, the hyperbolic nature of Eqs. (48c) and (48d) renders them amenable to another self-similar transform by the methods of characteristics. Defining $T = -\ln \tau$, one obtains along each characteristic defined by

$$\frac{d\xi}{dT} = \frac{1}{2}(2V + \xi), \tag{49}$$

the stress evolution

$$\frac{dX}{dT} = (2V_\xi - 1)X \quad \text{and} \quad \frac{dY}{dT} = -(V_\xi + 1)Y. \tag{50}$$

We shall carry out Taylor expansion in $\xi$ about the pinch-off stagnation point $\xi = \xi_0$ to facilitate numerical solution of Eqs. (48a) and (48b). However, as in the Newtonian case, the coefficients in the kinematic equation [Eq. (48b)] stipulate that the expansion is only possible (a smooth self-similar solution only exists) if

$$V_\xi(\xi_0) = 2, \quad V + \xi_0/2 = 0. \tag{51}$$

Hence, the leading-order expansion of the velocity is specified

$$V \sim -\xi_0/2 + 2(\xi - \xi_0). \tag{52}$$

The axial velocity is again a uniaxial extensional flow which flows to the right and left from the stagnation point $\xi_0$. However, unlike a straight-filament extensional flow, its strength increases in time, $u \sim 2\tau^{-3/2}(x - x_0)$.

Substituting Eq. (52) into Eq. (50), one again concludes that the radial excess stress approaches zero as the pinching progresses, $T \to \infty$ and $\tau \to 0$. The axial excess stress, however, increases monotonically as described by

$$\frac{dX}{dT} = 3X. \tag{53}$$

As for the characteristic lines during initial stretching, the characteristic lines on the plane of the self-similar variables $\xi$ and $T$ also fan out from the stagnation point $\xi_0$. Hence, the elastic stress near the pinching point is dominated by the evolution on the characteristic lines near $\xi = \xi_0$. Substituting the expansion of the velocity near $\xi_0'$ in Eq. (52) into Eq. (49), we get

$$\frac{d\xi}{dT} = \frac{5}{2}(\xi - \xi_0). \tag{54}$$

Combining Eqs. (54) and (53), it is clear that any initial stress profile $F(\hat{\xi})$ near $\xi_0$ at $T = 0$ would be propagated by the characteristics to produce a stress field $X(\xi,T) = F(\hat{\xi}e^{-5T/2})e^{3T}$ where $\hat{\xi} = \xi - \xi_0$ is the distance from the stagnation point. Expanding $X(\xi,\tau)$ in powers of $\hat{\xi}$, we obtain

$$X(\xi,\tau) = F(\hat{\xi}e^{-5T/2})e^{3T} \sim F_0(\tau) + F_2(\tau)\hat{\xi}^2, \tag{55}$$

where $F_0(\tau) = F(0)\tau^{-3}$ and $F_2(\tau) = \frac{1}{2}F''(0)\tau^2$. Hence, knowing the initial profile $F(\xi)$ for $X$, we can derive the time-dependent coefficients $F_i(\tau)$.

The dominant stress behavior near $\xi_0$ from Eq. (55) suggests the invariant scaling $\hat{\tau}_{zz}(t_0 - t)^4$ is the true self-similar transform for the pinching dynamics of the current viscoelastic jet. This is distinctly different from the $\hat{\tau}_{zz}(t_0 - t)$ scaling of a Newtonian jet from Eq. (47). The deviation originates from the $e^{3T}$ factor of Eq. (55) which, in turn, arises from the hyperbolic stress convection and elastic stretching enhancement. The universal stress scaling during self-similar pinching of a viscoelastic jet is hence quite distinct from that of a Newtonian jet eventhough the radius and velocity scalings of Eq. (47) are identical.

In Figs. 18 and 19, we verify these universal scalings of the pinching dynamics in a viscoelastic jet by collapsing both the stress evolution and the interface evolution at neck by demonstrating that, at the neck

$$\hat{\tau}_{zz} = \frac{\hat{\tau}_{zz}(0)t_0^4}{(t_0 - t)^4}, \quad h = \frac{H_{\min}}{SCa}(t_0 - t), \tag{56}$$

where $H_{\min}$ is a universal constant. The neck radius scaling is identical to that of a Newtonian jet for which Brenner et al.[6] have determined $H_{\min}$ to be 0.0304. The stress scaling, however, is unique to viscoelastic jets. In fact, the Newtonian scaling $\hat{\tau}_{zz} = \hat{\tau}_{zz}(0)t_0/(t_0 - t)$ fails to collapse the stress evolution in Fig. 18(a).

It would be difficult to solve Eq. (48) with expansion (55) to obtain the actual radius and stress profiles. Fortu-
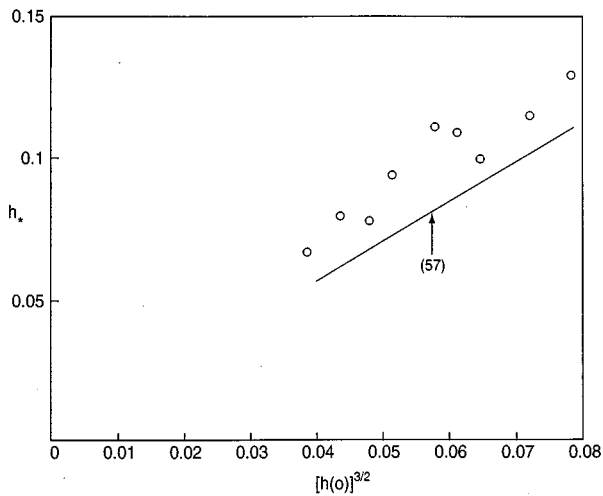
FIG. 20. Comparison of the predicted filament radius iteration $h_*$ $=\sqrt{2}[h(0)]^{3/2}$ from various experiments with varying conditions by triggering the recoil in Fig. 17 at different radius of the primary filament.

nately, scalings (56) are already sufficient for our purpose. Consider a primary filament in drainage, with stress $\hat{\tau}_{zz}(0)$ and radius $h(0)$, when its neck recoils due to bead disturbances. We do not know the values of $\hat{\tau}_{zz}(0)$ and $h(0)$ precisely, as they are determined by the disturbances as shown in Fig. 17. However, we do know they are related through the stretched filament correlation (34) from the neck analysis (that specifies the driving force during drainage) $Cah(0)\hat{\tau}_{zz}(0)=2$. We have set $t=0$ to be the onset of recoil and hence to be consistent, Eq. (56) must yield $t_0$ $=[h(0)SCa]/H_{min}$. The scalings (56) can now be inserted, with these matching conditions into the force balance (45) to determine the radius of the secondary filament. Consistent with our earlier leading-order matching in time, we use the self-similar recoil stress and radius of Eq. (56) in the subsequent quasi-steady force balance of the secondary filament in Eq. (46) during its stretching interval. Although $H_{min}$ is not known exactly, the power-law expressions allow us to eliminate $H_{min}$, $t_0$, $SCa$, $\hat{\tau}_{zz}$ and $\hat{\tau}_{zz}(0)$, to yield an explicit relationship between $h_*$, the radius of the secondary filament after the recoil and stretching stages but prior to elastic drainage, and $h(0)$, the radius of the primary filament when the recoil initiates

$$h_* = \sqrt{2}(h(0))^{3/2}. \tag{57}$$

This simple correlation is verified numerically in Fig. 20 by triggering the recoil in Fig. 17 at different radius $h(0)$ of the primary filament during drainage. The recoil is initiated by placing localized disturbances at the bead.

## VIII. DISCUSSION

The beads do not participate actively during the stretching and drainage stages. They act as sources of noise, or accumulators and transmitters of noise from the surrounding fluid, that trigger the recoil dynamics. However, they are unaffected by the recoil and the subsequent formation of the secondary filament. We hence expect this secondary filament to drain like the primary one as described by Eq. (37), but

with $h_*$ replaced by Eq. (57). We also expect it to suffer the same instability at the neck as the primary one, as captured in Sec. VI. An iterated stretching sequence is hence predicted, creating finer and finer filaments, even though we are unable to capture the higher-generation filaments numerically. If the disturbances are large, such that the recoil initiates before significant drainage has taken place, the filament radius is a constant and $h(0)$ in Eq. (57) corresponds to the undrained filament. From the drainage history of Figs. 6 and 17, this requires very little disturbance at the bead and is quite reasonable for a jet in the presence of constant noise from the environment. In this realistic limit, Eq. (57) yields a recursive relationship for filaments of successive generation

$$(r_n/r_0) = \sqrt{2}(r_{n-1}/r_0)^{3/2}, \tag{58}$$

in dimensional filament radius $r$ and the original jet radius $r_0$. Equivalently, if we allow the first iterate to be given by Eq. (30) and all subsequent ones by Eq. (58), one obtains

$$(r_n/r_0) = \left[\frac{Ca(1-S)}{We}\right]^{3(n-1)/4}, \tag{59}$$

and the axial elastic stress of the $n$th filament, from Eq. (34),

$$\hat{\tau}_{zz}(n) = \frac{2}{Ca}\left[\frac{Ca(1-S)}{We}\right]^{-3(n-1)/4}. \tag{60}$$

The elastic stress hence increases very rapidly with each successive filament, as we have observed in Fig. 18 for just one iteration. As the elastic stress increases, so does the polymer stretching $A$ is the axial direction, as described by the Oldroyd-B model. Eventually, $A \sim L^2$ in the spring law (2) and extensibility becomes important. As seen in Fig. 9, a low-$L$ primary filament, analogous to a high-generation filament, will no longer recoil and the iteration ceases. Breakup is expected at that point.

The above universal scalings arise from the asymmetric self-similar pinching after recoil. This particular self-similar solution necessarily involves inertia, as does Egger's for Newtonian jets.[2] In fact, it is the ony stage where inertia is important. We have carried out simulations by artificially removing the inertial terms. Only the pinching dynamics after recoil differ from those with inertia. The recoil still initiates at the neck as the Rayleigh instability responsible for triggering it is independent of inertia. A secondary filament still forms but it does not obey correlation (57). The pinching is also asymmetric, unlike the inertialess pinching of Papageorgiou's solution[4] for Newtonian jets without inertia. We are hence unable to predict the radius of the secondary filament if inertia is omitted. However, as is evident from the naturally scaled governing equations [Eq. (9)], inertia is negligible for a jet surrounded by an inviscid fluid only for excessively small $Ca$ and $S$ in the limit of large $We$. This is impractical and we expect inertia to enter during the pinching and recoil at the neck, as we have observed in our simulations. In fact, to obtain Papageorgiou's symmetric pinching solution, one must introduce large-amplitude disturbances at the middle of the filament that will transform the linear uniaxial extensional flow into a uniform axial flow with vanishing $(\partial u)/(\partial z)$. Only then would the inertial term
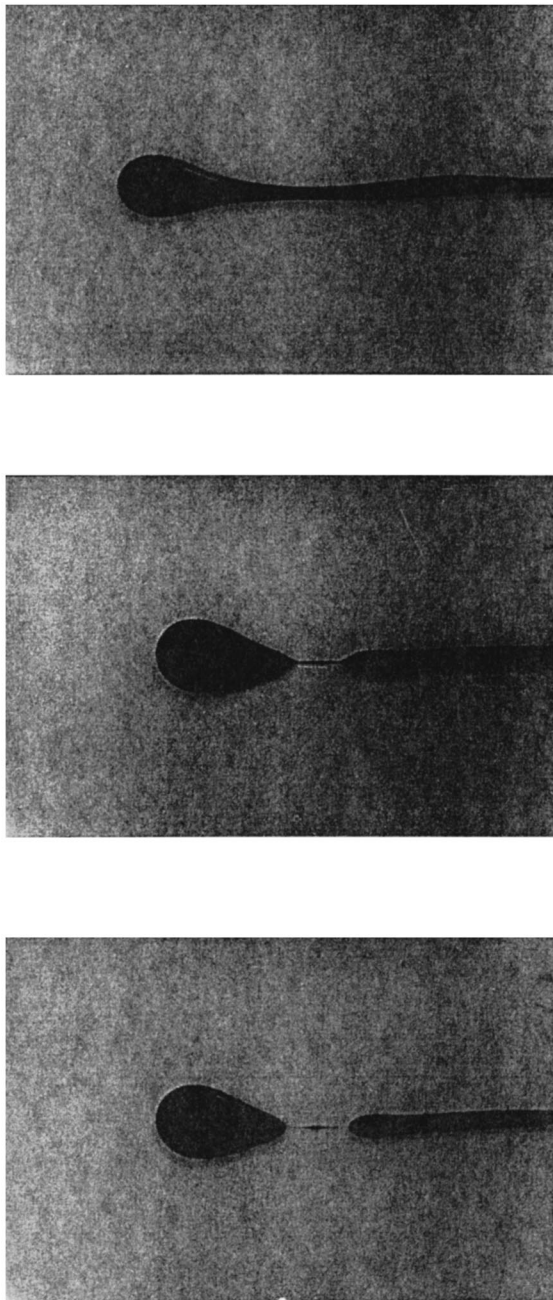
FIG. 21. Photographs taken from a primitive experiment in which a viscoelastic bead-filament configuration is created in a Newtonian fluid of the same density. The photographs are taken with about 20 s intervals. The primary filament clearly stretches, recoils, and restretches to form a secondary filament.

$u(\partial u)/(\partial z)$ in Eq. (9a) be negligible. Hence, we expect inertia to be important for recoil and pinching at the neck for most practical values of $Ca$ and $S$ of a highly elastic jet ($We \gg 1$) in an inviscid surrounding. Since we have shown the neck is the most unstable portion of the stretched filament, we expect inertia to play an important role in the recoil and stretching iterations. In our simulations, we have only seen symmetric pinching for the singular limit of $S=1$. A consequence of this argument is that recoil may not occur for jets in a viscous fluid where inertia can be independently and artificially suppressed. However, such jets can trigger other

viscoelastic effects as their axial velocity has a radial gradient even in a straight filament. This scenario is beyond the current theory.

All prior experimental studies of the viscoelastic bead-filament configuration involve flying jets instead of static ones confined within finite domains. In a long flying jet, the beads can slide along the filaments[8] and disrupt the recoil dynamics. The jet also bends and twists when the bead-filament configuration appears. Not surprisingly, there is no reported observation of recoil and high-generation filaments. To remedy this, we have performed a primitive experiment by squeezing a viscoelastic fluid of uncharacterized rheological properties through a tube into a Newtonian fluid of about the same density but much lower viscosity. We have squeezed an excess of fluid initially to create a bead-like head followed by a narrower filament, as seen in Fig. 21. Despite the crudeness of the experiment, the filament stretches immediately by draining into the bead and undergoes a distinct recoil to generate a secondary filament. Note the recoiled primary filament forms another bead-like structure that bounds the other end of the secondary filament. This suggests that recoils and stretchings to form high-generation filaments are to be expected from viscoelastic jets. More careful experiments are underway to verify the universal scalings of Eq. (58).

## ACKNOWLEDGMENTS

[1] N. N. Mansour and T. S. Lundgren, ''Satellite formation in capillary jet breakup,'' Phys. Fluids A **2**, 114 (1990).
[2] J. Eggers, ''Universal pinching of 3D axisymmetric free-surface flow,'' Phys. Rev. Lett. **71**, 3458 (1993).
[3] J. Eggers, ''Theory of drop formation,'' Phys. Fluids **7**, 941 (1995).
[4] D. T. Papageorgiou, ''On the breakup of viscous liquid threads,'' Phys. Fluids **7**, 1529 (1995).
[5] M. P. Brenner, X. D. Shi, and S. R. Nagel, ''Iterated instabilities during droplet fission,'' Phys. Rev. Lett. **73**, 3391 (1994).
[6] M. P. Brenner, J. Lister, and H. A. Stone, ''Pinching threads, singularities and the number 0.030...4,'' Phys. Fluids **8**, 2827 (1996).
[7] M. P. Brenner, J. Eggers, K. Joseph, S. R. Nagel, and X. D. Shi, ''Breakdown of scaling in droplet fission at high Reynolds number,'' Phys. Fluids **9**, 1573 (1997).
[8] M. Goldin, J. Yerushalmi, R. Pfeffer, and R. Shinnar, ''Breakup of a laminar capillary jet of a viscoelastic fluid,'' J. Fluid Mech. **38**, 689 (1969).
[9] R. Keunings, J. Comput. Phys. **62**, 199 (1986).
[10] D. W. Bousfield, R. Keunings, G. Marrucci, and M. M. Denn, ''Nonlinear analysis of the surface tension driven breakup of viscoelastic filaments,'' J. Non-Newtonian Fluid Mech. **21**, 79 (1986).
[11] M. Renardy, ''A numerical study of the asymptotic evolution and breakup of Newtonian and viscoelastic jets,'' J. Non-Newtonian Fluid Mech. **59**, 267 (1995).
[12] V. M. Entov and E. J. Hinch, ''Effect of a specturm of relaxation times on the capillary thinning of a filament of elastic liquid,'' J. Non-Newtonian Fluid Mech. **72**, 31 (1997).
[13] M. Renardy, ''Some comments on the surface-tension driven break-up (or lack of it) of viscoelastic jets,'' J. Non-Newtonian Fluid Mech. **51**, 97 (1994).
[14] M. D. Chilcott and J. M. Rallison, ''Creeping flow of dilute polymer solutions past cylinders and spheres,'' J. Non-Newtonian Fluid Mech. **29**, 381 (1988).

[15]R. B. Bird, R. A. Armstrong, and O. Hassager, *Dynamics of Polymeric Fluids* (Wiley, New York, 1977), Chap. 10, pp. 471–510.

[16]M. J. Soloman and S. J. Muller, ''Flow past a sphere in polystyreme-based Boger fluids: the effect on the drag coefficient of finite extensibility, solvent quality and polymer molecular weight,'' J. Non-Newtonian Fluid Mech. **62**, 81 (1996).

[17]S. Kalliadasis and H.-C. Chang, ''Drop formation during coating of vertical fibers,'' J. Fluid Mech. **261**, 135 (1994).

[18]J. Ratulowski and H.-C. Chang, ''Transport of gas bubbles in capillaries,'' Phys. Fluids A **1**, 1642 (1989).

[19]P. Huerre and P. A. Monkewitz, ''Local and global instabilities in spatially developing flows,'' Annu. Rev. Fluid Mech. **22**, 473 (1990).